Challenges in Scaling Down of Free-Floating Implantable Neural Interfaces to Millimeter Scale

KAI-WEN YANG[1]**, (Student Member, IEEE), KEONGHWAN OH**[1,2]**, (Student Member, IEEE), AND SOHMYUNG HA**[1,2]**, (Member, IEEE)**
[1]Division of Engineering, New York University Abu Dhabi, Abu Dhabi, United Arab Emirates
[2]Tandon School of Engineering, New York University, New York, NY 10003, USA

Corresponding author: Kai-Wen Yang (kwy225@nyu.edu)

ABSTRACT Implantable neural interface devices are an emerging technology for continuous brain monitoring and brain-computer interface (BCI). Recording of electrical signals from neurons of interest has led to more efficient and personalized diagnosis, treatment, and prognosis of neurological disorders. It facilitates the dynamic mapping of the whole brain, improving our understanding of the links between brain functions and behaviors. Stimulation of targeted nerves and neurons has been utilized as an effective therapy for Parkinson's disease, essential tremor, dystonia, etc. It has also been developed as motor neuroprosthetic devices, improving the quality of life of many. Although initial designs were bulky, recent advances in semiconductor and nano-, micro-technology has enabled the miniaturization of such devices to the millimeter scale. Free-floating neural implants of miniature size are highly scalable to be distributed around the targeted region of interest more extensively. They are more clinically viable as they cause less disturbance to the body and induce less tissue immune response. However, these research efforts for scaling down have faced challenges resulted from decreasing the size of such implants, including issues pertaining to wireless powering, data communication, neural signal recording, and neural stimulation. Through extensive literature research and simulations, the limits and trade-offs regarding neural implant miniaturization are investigated and analyzed for each aspect of the challenges. State-of-the-art development and future trends for advanced neural interfaces are also explored.

INDEX TERMS Implantable neural interface, neural signal recording and stimulation, wireless power transfer, millimeter size, free-floating neural probes.

I. INTRODUCTION

Implantable neural interfaces with recording and stimulation functionalities have the potential to bring about transformative changes in medical and research applications. In the field of medicine, more effective and personalized disease prevention, diagnosis, prognosis, and treatment can be achieved with continuous monitoring of neural signals. Therapeutic electrical stimulation, the induced alternation of brain activity through delivering electrical impulses to targeted brain areas, has been regarded as an effective therapy for treating Parkinson's disease [1], essential tremor [2], dystonia [3], obsessive-compulsive disorder (OCD), major depressive

disorder (MDD) [4], and epilepsy [5]. More recently, brain-computer interface (BCI) or brain-machine interface (BMI) has been developed as motor neuroprosthetic device [6], [7], which could significantly promote the quality of life for those with serious motor impairments, such as spinal cord injury, stroke, and limb loss [8]. In research, such technology can help us picture how individual neurons and neural circuits work in the whole brain scale and discern how our brain processes, stores, and retrieves information [9]. All applications mentioned above require closed loop neural interface systems capable of reliably recording from the brain and delivering electrical stimulation to the targeted location.

The demand for wirelessly powered neural interfaces has increased significantly as they do not require batteries and the subsequent need for battery replacement surgeries. The risk

The associate editor coordinating the review of this manuscript and approving it for publication was Gang Wang.

of infection can also be predominantly decreased as percutaneous wire connections are eliminated. Most neural systems powered wirelessly rely on microelectrode arrays (MEA) to interface with neurons [10], such as the Michigan [11] and Utah [12] arrays. Another emerging approach to improve specificity and scalability utilizes CMOS technology to overcome spatial routing constraints on the electrode-pad of the probe [13], [14]. Example systems with such design include the Neuroseeker [15], Neuropixels [16], [17], and SiNAPS, which to date can achieve 83 recording channels per mm^2 total silicon area of the probe [13]. However, the major shortcoming of such systems is their strict limit on the location and configuration for neural recording and stimulation [18]. Though high channel counts can be achieved, it cannot be widely deployed at several regions of the brain due to its centralized approach. MEAs are ideal for applications that require localized coverage, but less desirable for those that prioritize the need for wider distribution. Representative applications with such need include treating neurological disorders that affect distributed locations [19] and engaging neurons of larger areas to achieve more accurate control of robotic prosthetic limbs [20]. To that end, free-floating implantable neural systems that enable a more distributed neural interface have gain wider attraction. Probes of lower or single channel count coupled with minimized operating elements allow them to be distributed across the surface of the cortex, which not only expands the reachable region in the brain, but also makes it scalable up to more than thousands of channels.

While the prospect of fully wireless free-floating implantable neural interfaces is propitious, their sizes remain one of the major hindrances to its advancement and application. Firstly, there is very limited space available in the brain as disparate tissues and structures are compactly layered. Secondly, larger implants have brought about significant tissue immune responses, while the smaller and untethered ones induce smaller reactions [21], [22]. Undesirable brain immune responses against implants will not only significantly impact signal sensitivity and clarity and the sensor's life time, but also endanger patient's health and well-being [23]. Smaller implants also require smaller surgical area, which translates into less complicated surgery, lower risk, and shorter recovery time. Furthermore, due to the relatively massive size of the implants (when compared to the scale of a neuron), electric impulses targeted toward a certain nerve group might ended up indiscriminately co-stimulating neighboring nerves, leading to undesirable side effects [24]. For instance, DBS for Parkinson's disease inadvertently affects adjacent nerves that are not related to movement control, resulting in unwanted symptoms such as paresthesia and nausea [25]. Vagus nerve stimulation (VNS) delivers electrical impulses to the whole vagus nerve, which contains around 100,000 neural fibers, each having various functions and connecting to different organs [24], [26]. As the implant size is reduced, they can be placed on the targeted location of interest, therefore recording and stimulating the target
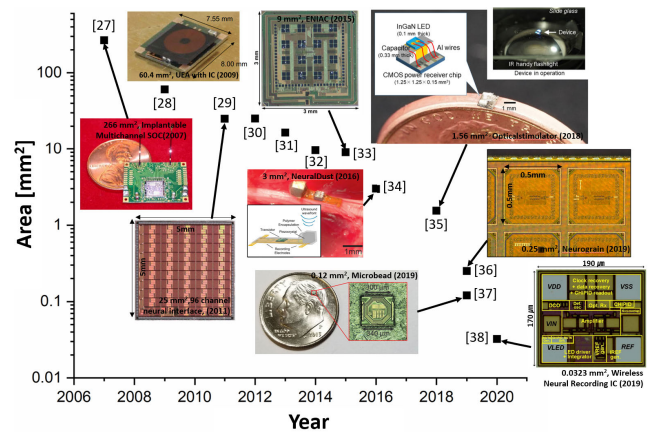

FIGURE 1. Scaling-down trend of implantable neural interfaces to millimeter scales over the years [27]–[38] .

sites with higher spatial specificity. As a result, researches in the field of fully wireless free-floating neural implantable interfaces strive to minimize the footprint of such devices. As seen in Fig. 1, the sizes of neural implants developed have decreased from more than 100 mm^2 in 2007 to less than 0.1 mm^2 in 2020.

While the imperativeness of scaling down neural implants to millimeter or even sub-millimeter scale is indisputable, physical, physiological, and technological challenges remain and require to be overcome. The following sections discuss the emergent challenges of scaling down of millimeter-scale implantable neural interfaces, including power transmission and harvesting, communication, neural signal recording, and neural stimulation. Various state-of-the-art fully wireless free-floating modular systems are explored and discussed, followed by the delineation of the future outlook of this field.

II. POWER TRANSMISSION AND HARVESTING

Recent progresses in semiconductor microelectronics have given rise to the prosperous development of low-power bioelectronics. However, active elements within circuits still require substantial power to detect neural signals, process and transmit recorded data to external devices. Power is an even more crucial element for implants with stimulating functions due to its high-energy requirement.

Since the advent of implantable medical devices (IMDs) in the late 1950s, batteries have long been the major power source for IMDs [39]. Using batteries as the power source exempts such devices from wired operation that may expose the internal tissue to the extracorporeal environment, which is considered unsafe and prone to infections. Nevertheless, the use of battery imposes several limitations, rendering it a less desirable and sustainable power source. To begin with, batteries have a finite lifetime and need to be replaced after depletion of the total stored energy [40]. As IMDs are usually placed deep inside the body, an invasive surgical operation is required to replace the battery after its depletion. Thus, patients are typically averse to it because of the accompanying risk, suffering, and long recovery time. Studies have

also shown that battery longevity decreases with successive replacements of implantable pulse generators, so batteries have to be altered even more frequently [41], [42]. In addition, unexpected premature depletion of the battery might lead to catastrophic malfunctioning of the device [43]. Though unlikely, there is also potential risks of leakage of electrolytes from the battery, whose toxic substances are especially detrimental if happened in the brain. Moreover, the advance of battery technology remains relatively stagnant. Batteries still occupy around 75% of the device [44], making it a bottleneck that hinders the minimization of IMDs while circuit elements have become significantly smaller due to recent rapid developments of integrated circuits (IC) [45]. With 1.0 Wh/cm^3 as the volumetric energy density of the lithium/iodine battery [46], the total available energy of varying battery volumes can be seen in Fig. 2 (black line). The lifetime of the battery depends significantly on the power consumption of the device, as shown by the blue lines each represent power consumption of $1~\mu$, $10~\mu$, $100~\mu$, and 1 mW. 36 J of total energy can be stored in the battery of 10 mm^3 volume, which can last for around 1 year when $1~\mu$W is consumed. On the other hand, only 0.36 J can be supplied for battery size of 0.1 mm^3, which translates to the lifetime of approximately 4 days with the identical power consumption condition. It can be clearly seen that as the size of the implant scales down, the total energy and lifetime of the battery proportionally decreases, which remains a grave challenge for supplying sufficient power for a long term.
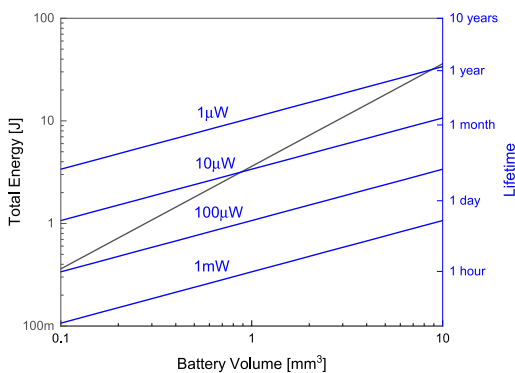

FIGURE 2. The relationship of the volume of the battery with the total energy (black line) and lifetimes for different power consumption (blue lines).

To extend the lifespan of batteries, the first rechargeable (RC) implantable neurostimulator was designed (Activa RC, Medtronic) and received FDA approval in 2009 [47]. Advantages brought by this innovation include slightly smaller size of the device due to a smaller battery, longer lifespan (lasts >10 years in comparison to 3-5 years in fixed-life batteries for DBS), and thus less frequent battery-replacement surgery. However, the battery has to be recharged on a regular basis, either 2-3 times per week each for 30 minutes, or charging it with longer duration and less frequency. This requires significant dedication, and failure to do so might

result in serious symptom recurrences. Owing to such pros and cons, the attitude toward this approach is inconclusive. Acceptance toward RC implants is high in some studies while 63% indicated fixed-life battery as a more preferable option in another study, due to convenience and concerns of forgetting to recharge the battery [48]–[50].

The constraints imposed by the use of batteries fostered the research and progress of powering schemes using contactless energy transfer (CET), which can be mainly categorized into two types. The first type is wireless power transmission (WPT) that includes components equipped with energy delivering and receiving capabilities with power being transmitted through either RF electromagnetic, ultrasonic waves, or infrared light. Rechargeable neural stimulating devices currently available in the market utilize wireless power transmission, mainly electromagnetic waves (EM), as the charging mechanism [51]. The second type involves energy-harvesting components that can obtain energy from the surrounding environment, either thermoelectrically, mechanically, or chemically. Although these methods sound attracting, sustaining sufficient power to miniature implants deep inside the brain without the use of batteries and wired connections is a great technological challenge. Each of these approaches comes with its own features, advantages, drawbacks, and challenges, which will be expounded further in the following subsections.

A. ELECTROMAGNETIC POWERING

Electromagnetic powering is one of the most developed, popular approaches for wireless energy transmission. Near-field inductive coupling and midfield wireless powering (MWP) are two of the main schemes for this application. Although near-field wireless powering is more widely used for medical implants due to its high power transfer efficiency (PTE), power delivered to load (PDL), and lower energy absorption in biological tissues with the use of lower frequency waves (< 0.5 GHz), some neural interfacing systems employ the mid-field method (Montgomery *et al.*, *Nature Methods*, 2015). Readers interested in knowing more about the intricacies and comparisons of the said methods can refer to Ho *et al.*, *Proceedings of the IEEE*, 2013 and Agarwal *et al.*, *IEEE Rev Biomed Eng*, 2017.

In power transfer system through inductive coupling, the primary coil generates an alternating magnetic field from an alternating power source as shown in Fig. 3. When a secondary coil is placed in proximity to the primary one and is inductively coupled, energy is transferred as delineated in Faraday's Law [52]. The PTE of such an inductive link is governed by the following equation:

$$PTE = \frac{k^2 Q_1 Q_{2,loaded}}{1 + k^2 Q_1 Q_{2,loaded}} \frac{R_{P,2}}{R_{L,ac} + R_{P,2}} \qquad (1)$$

where k is the coupling coefficient, Q_1 and Q_2 are quality factors of the transmitter and receiver coils, R_1 and R_2 are the equivalent resistance modeling the losses of the primary and
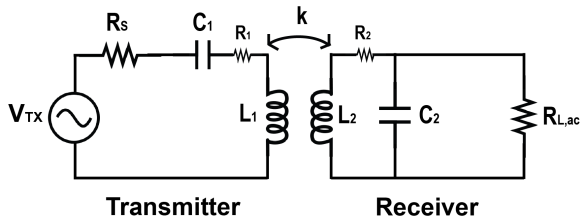
**FIGURE 3.** Simplified circuit model for typical inductive power transfer systems.

secondary coil, $R_{L,ac}$ is the load resistance. $Q_{2,loaded} = \eta_2 Q_2$, $\eta_2 = R_{L,ac}/(R_{L,ac} + R_{P,2})$, $R_{P,2} = R_2(Q_2^2 + 1)$ [53].

Inductive power transmission is considered a robust scheme for WPT as considerable energy can be delivered reliably. Well-designed systems can reach a PTE of 95% with air being the propagation medium [54], [55], and therefore has received the most attention. Inductive powering systems for battery recharging are currently commercially available; products applying this scheme include Activa RC (Medtronic), Activa PC+S (Medtronic), Brio (St. Jude) [56]. However, the high-absorption nature of biological media coupled with high-scattering characteristics of the multilayer structure result in great power attenuation which significantly compromises the power transfer efficiency. As such absorption generates heat and raises safety concerns, the maximum allowable power to be transmitted should comply with the specific absorption rate (SAR) limit, which is 1.6 W/kg according to the IEEE guideline [57]. Therefore, the maximum power density of electromagnetic (EM) waves is restricted due to potential harmful health effects resulted from excessive tissue heating [58], [59]. The output power density is dependent on the frequency of the EM wave and should not exceed 10 mW/cm^2 [34]. Furthermore, the high absorption rate of EM in both soft tissues and the skull brings about rapid decrease in PTE when the transfer distance is large. For instance, for an implantable coil ($25 \times 10 \times 0.5$ mm^3) powered at frequency of 13.56 MHz in tissue environment (porcine tissue), PTE of 58% can be achieved at a distance of 10 mm, yet it drastically degenerates to 0.16% at 50 mm [60]. At 500 MHz, the attenuation values for fat and muscle tissue were reported to be 1.66 dB/cm and 4.60 dB/cm [61]. As this approach necessitates close coupling between the two coils, it is very sensitive to misalignment, which can significantly compromise the PTE.

The coupling coefficient k and quality factor Q are the two major determinants of power transfer efficiency through EM waves, and both parameters are gravely compromised when the coil antenna size is scaled down. The achievable Q factor becomes lower as current CMOS technology can typically support a top metal thickness of 1-4 μm [62]. The smaller coil geometry combined with large separation distance both contribute to lower coupling coefficient. For millimeter-scale free-floating implants, achievable Q factor is typically less than 10, achievable k is around 0.005 and the resulting PTE is only 2% or less [62]. With operating

frequency of 144 MHz, receiver coil size of 8.64 mm^2, and coil separation distance of 10 mm (porcine fatty abdominal tissue), 2.04% of WPT system efficiency was achieved [63]. As the size of the implant is reduced, the antenna size decreases, which inevitably brings about the decrease in both PTE and PDL. Furthermore, the decrease in antenna size also leads to the increase in the optimal frequency for its operation. Yet since tissue absorption is greater at higher frequencies, the transmittable power consequently becomes lower.

To demonstrate this challenge, a multilayer brain tissue model with frequency-dependent dielectric properties was constructed using the 3D finite element method (FEM) simulator (Ansys HFSS), as seen in Fig. 4 (a) [64]. An external single-turn coil with 12-mm radius for power transmission was positioned concentrically with the implant coil above the skin with an air gap of 1 mm. The implant, which was assumed to be a 200 μm-thick semiconductor chip fabricated in a CMOS Silicon-on-Insulator (SOI) process (XFAB 180 nm), was covered with Parylene C and placed on the grey matter under the skull at a depth of 9.7 mm. The receiver coil on the implant has dimension $D \times D$, which was varied from 0.1×0.1 to 10×10 mm^2 (Fig. 4 (b)). It was constructed with varying number of turns n (1-7 turns) in the identical layout ratio. The widths (t) of the coil metal and gap are kept at 1:1, while t varies depending on D and n, as generalized by the
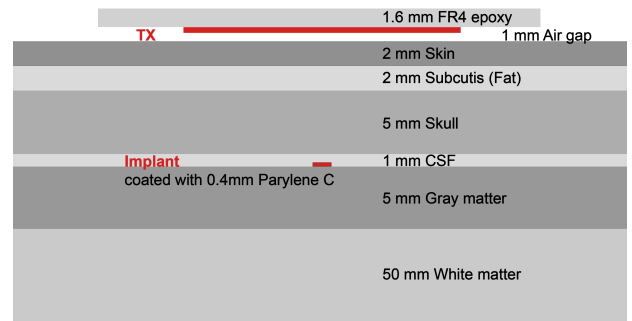
(a)
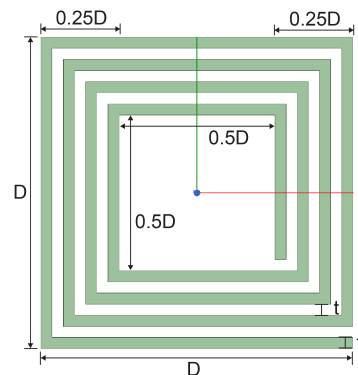
(b)

FIGURE 4. (a) The cross section configuration of the employed FEM simulation model in HFSS. (b) The schematic of the on-chip coil antenna as part of the implant. A representative 4-turn coil is shown here while 1- to 7-turn coils are constructed in the simulation.
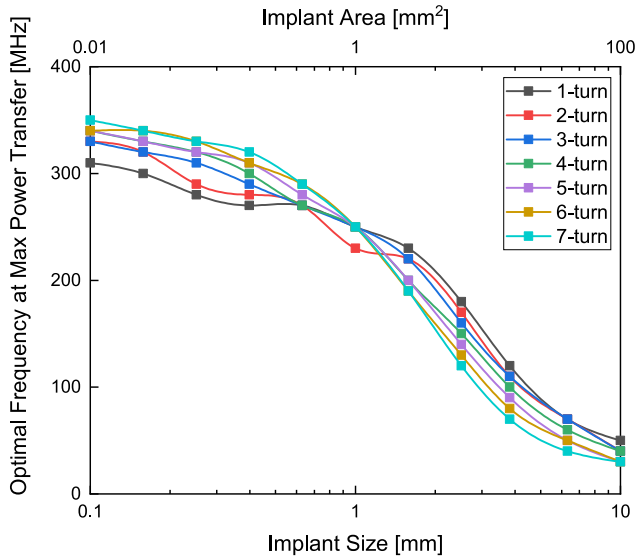
FIGURE 5. The optimal frequency for various implant sizes and number of receiver coil turns under the load condition of maximum power transfer.

following equation:

$$0.25D = (2n - 1) \times t \tag{2}$$

As an example, Fig. 4 (b) shows the schematic of the on-chip antenna of a 4-turn coil.

The model was simulated with various frequencies to identify the conditions that result in the maximum PTE, through which the optimal frequency for power transfer was determined. Under the condition of maximum power transfer, in which the load is assumed for the maximum power transfer, the resulting optimal frequencies for various sizes and number of turns can be seen in Fig. 5. As shown, both the optimal frequency and number of coil turns increase as the size of the implant decreases. Power transfer frequency of around 310-350 MHz is optimal for implant size of 0.1 mm (area of 0.1×0.1 mm^2) while that decreases to 250 MHz for 1 mm (1×1 mm^2) and approximately 30-50 MHz for 10 mm (10×10 mm^2). Fig. 6 illustrates the relationships between various parameters and implant size after the number of turns was optimized. It can be discerned from both Fig. 6 (b) and (c) that the coupling coefficient and maximum PTE decrease significantly as the implant size reduces. The maximum achievable coupling coefficient is 0.043 for implant size of 10 mm, which decreases to 1.36m for 1 mm (a 32-fold decrease) and 0.068m for 0.1 mm (another 24-fold decrease). PTE of up to 23% can be achieved for implant size of 10 mm, while that drastically deteriorates to 0.036% for 1 mm (a 639-fold decrease) and 5.98μ% for 0.1 mm (another 6053-fold decrease). The decrease in slope of the maximum PTE (+16.5 dB/decade for implant area) is approximately twice that of the coupling coefficient (+7 dB/decade). This is in accordance with the fact that PTE is roughly proportional to k^2 when k is very small, as illustrated in Eq. (1).

However, the assumption of maximum power transfer is far from realistic and the PTE is a strong function of load resistance (R_L) [53], which should also be taken into account when conducting parameter optimization. To achieve this, an optimal frequency was selected for a specific implant size and the transmittable power was maximized under the 1.6W/kg SAR constraint. The relationships between the maximum PDL and the load resistance for implant sizes 0.1×0.1, 1×1, 10×10 mm^2 are shown in Fig. 7. Significant differences in the magnitudes of PDL for implants of various sizes were observed: PDL is in the nW-pW range for 0.1 mm, the 0.1-100s μW range for 1 mm, and 1 mW to unit-digit watt for 10 mm. For the smaller implant size of 0.1 mm, the 7-turn coil dominates throughout the range of interest while this trend in dominance changes as the implant size increases. The 7-turn coil also dominates throughout the whole sizes of interest with load resistances larger than 10 kΩ. These simulation trends can be validated with derivations as delineated below. For large implant sizes, with $Q_2^2 = L_2/(C_2 R_2)$ and $Q_2^2 \gg 1$ for the range of interest, Eq. (1) can be simplified to the following:

$$PTE \cong \frac{k^2 Q_1 Q_2 \frac{R_L}{R_L + L_2/C_2}}{1 + k^2 Q_1 Q_2 \frac{R_L}{R_L + L_2/C_2}} \frac{L_2/C_2}{R_L + L_2/C_2} \tag{3}$$

For large R_L ($R_L \gg L_2/C_2$), Eq. (3) can be further simplified to the following expression:

$$PTE_{large\ R_L} \cong \frac{k^2 Q_1 Q_2}{1 + k^2 Q_1 Q_2} \frac{L_2}{R_L C_2} \tag{4}$$

Eq. (4) shows that the PTE is inversely proportional to R_L. As seen from the right-hand side of Fig. 7 (c), the higher the load resistance is, the lower the PTE is. In addition, as the number of coil turns increase, L_2 increases while C_2 decreases, resulting in a net increase in the L_2/C_2 factor. Since the PTE under this scenario is proportional to L_2/C_2, the coil of higher turns (7-turn) dominates. On the other hand, for smaller R_L ($R_L \ll L_2/C_2$), Eq. (3) can be further simplified to the following expression:

$$PTE_{small\ R_L} \cong k^2 Q_1 Q_2 \frac{R_L C_2}{L_2} \tag{5}$$

Eq. (5) shows that the PTE is proportional to R_L as seen from the left portion of Fig. 7 (c). Since the PTE is proportional to C_2/L_2 in this scenario, which is the inverse of the previous case, the coil of lower turns dominates. The derivation above can also be applied to the case of smaller implant sizes. $R_L \gg L_2/C_2$ holds true for smaller implant coils since they have smaller L_2 and larger C_2 values. The PTE under this scenario can be approximated by Eq. (4) and exhibit trends akin to that described in the first case. Fig. 7 (a) shows that PTE is inversely proportional to R_L and that the 7-turn coil dominates throughout the simulation range. Fig. 8 shows the optimal number of turns across various implant sizes for representative load resistance values of 0.1, 0.4, 0.7, 1, and 10 kΩ. This demonstrates that the optimal number of turns depends strongly on the load resistance and the implant size, and therefore, both should be considered when determining the optimal scenario.
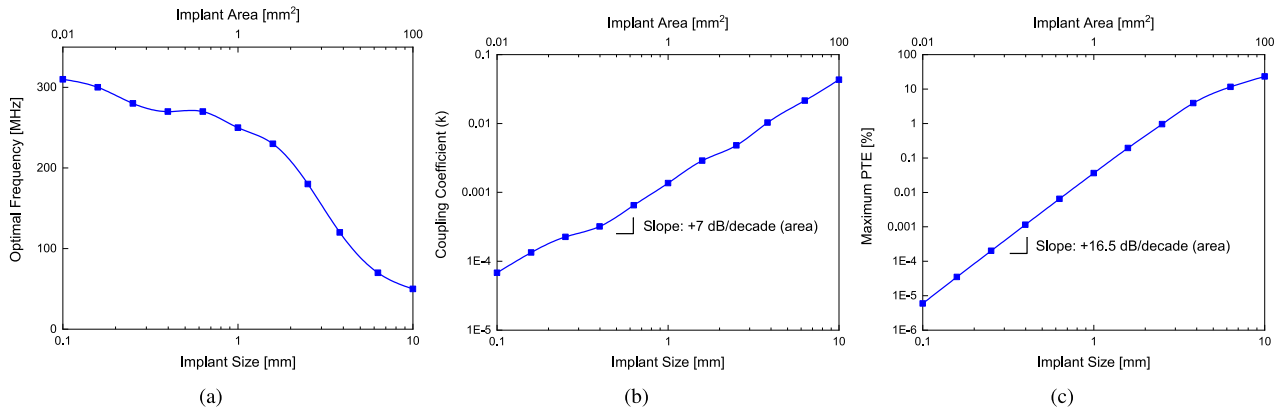
FIGURE 6. Under the load condition of maximum power transfer, the relationships of the implant size with (a) optimal frequency, (b) coupling coefficient, and (c) maximum PTE.
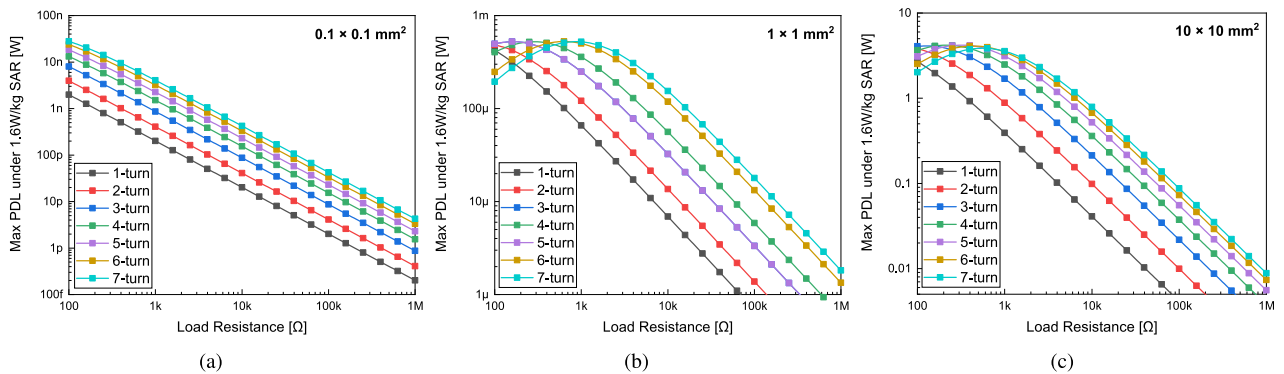

FIGURE 7. The relationships between the maximum PDL and load resistance for various number of turns and implant sizes of (a) 0.1×0.1 mm^2 (b) 1×1 mm^2, and (c) 10×10 mm^2.
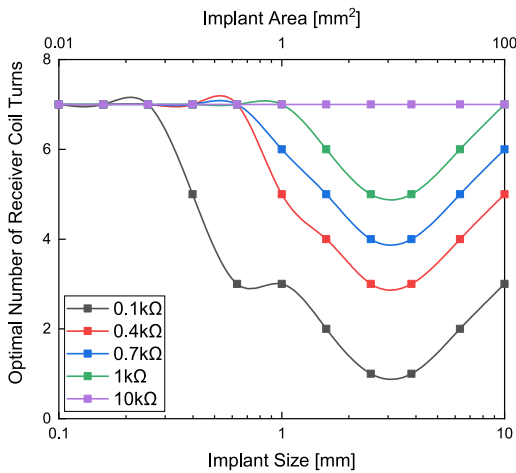

FIGURE 8. The optimal number of turns for the receiver coil across various implant sizes for load resistance values of 0.1k, 0.4k, 0.7k, 1k, and 10kΩ.

To mitigate adverse effects mentioned above, researchers have proposed several designs to increase PTE as delineated in the following section.

1) COIL FABRICATION ON THE IMPLANT SIDE

The Q factor of the implant coil crucially determines k and PTE of the WPT to the implant. There are three

schemes for the receiver coil structure in millimeter-scale implants: in-CMOS (fully integrated in the substrate), above-CMOS (adhered on top of the substrate), and around-CMOS (wires wounded around the chip). The around-CMOS scheme achieved both the highest Q factor of 26.23 (at 283MHz) and SAR-constrained maximum PTE of 3.05% (at 318.8MHz) among the three approaches [62]. To fabricate such structure, the insulated bondwire is wound around the passive silicon die with the manual wire-bonder (Westbond 7476D, Anaheim, CA) and stepper motor [65]. On top of the conventional 2-coil inductive link, schemes of multiple-coupled inductive link have also been proposed. The 3-coil inductive link, with an additional coil (resonator) added underneath the dura matter, was demonstrated to have the highest PTE (9.13% at 275MHz in tissue media) and power delivered to load (PDL) in comparison to its 2-, 4-coil counterparts [66], [67].

2) TRANSMITTER DESIGN

To more effectively focus energy that is transmitted from air through heterogeneous tissues in the human body, a conformal device with ring-shaped metal strips fabricated on a silicon substrate is designed [68]. It utilizes the interference of the waves radiated from various metal strips that are oscillating at different phases to focus energy. It has been demonstrated to increase the robustness of the system to both

the changes in surface properties and the heterogeneity of the mediums the wave passes through.

Segmentation of the transmitter antenna was also shown to increase the uniformity of the current distribution and PTE while lowering SAR. This is achieved through preventing phase-inversion in the current distribution along the coil that causes electromagnetic field cancellation [69]. It was demonstrated through HFSS simulations that the 3-coil transmission link with segmented coils leads to less SAR than that with unsegmented ones [70].

To enable the simultaneous optimization of both the power and data transmission link, schemes of separating the power and data coil have been proposed. PTE can be maximized for high Q links and low frequency to minimize losses while data transfer efficiency is maximal for low Q links and best be achieved through higher frequency [71].

B. ULTRASONIC POWERING

Ultrasonic powering utilizes ultrasonic waves, an oscillating sound wave beyond the hearing range of human, to deliver energy wirelessly. Ultrasonic powering devices are composed of two transducers made with piezoelectric materials to transmit and receive energy, respectively. An external transmitting transducer converts electrical energy into a pressure wave that propagates through tissues. An internal receiving transducer then converts the mechanical vibration caused by the acoustic wave back to electrical energy, which is then rectified to provide a stable DC voltage to power the load [72].

Although this approach received less attention in comparison to electromagnetic waves for powering medical implants, it has recently become more popular due to its numerous advantages. As ultrasound has long been used in biomedical fields, such as ultrasound imaging and rehabilitation, its safety is more warranted. Due to its much lower propagation velocity, considerably shorter wavelength under the same frequency can be achieved than that of EM waves. Hence, the size of the transmitter and receiver can be several orders smaller, ideal for scaling-down of implants [73]. On the other hand, when the dimension of the device is set, the frequency used through ultrasonic powering can be a lot lower than electromagnetic waves. As a result, power attenuation of the wave in soft tissue is substantially smaller than EM waves, leading to deeper tissue penetration. According to simulation results after optimizing geometric parameters for both EM and ultrasonic power transfer, ultrasonic system demonstrates better power transmission efficiency when the receiver diameter is minimized down to 2 mm in both cases of 1 cm and 10 cm transmitter-receiver separation distance, as shown in Fig. 9 [45]. Its feasibility has also been demonstrated through *in-vivo* experiments [34], [74]. Ultrasonic systems are also more efficient in focusing energy at the mm-scale. According to [75], for small receiver dimensions of 1.1 mm^3 simulated in homogeneous environment (muscle for the inductive link and soft tissue for the ultrasonic link), PTE of 10.6%, 0.7% and PDL of 2 mW, 1 mW can be achieved for 10-mm and 50-mm implant depth, while that for the inductive
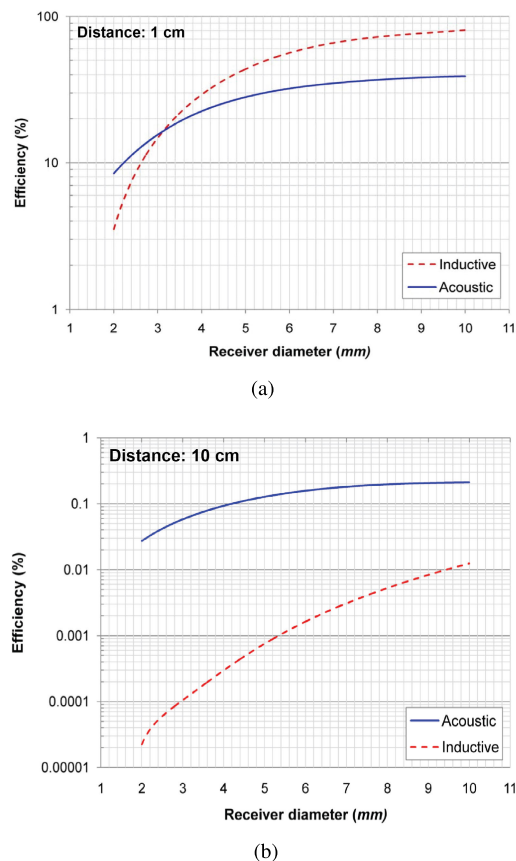

FIGURE 9. Simulation results of PTE in soft tissues for inductive and acoustic powering as a function of receiver diameter when the separation distance of the power and implant is (a) 1 cm and (b) 10 cm [45].

link are 3.65%, 0.0064%, and 0.88 mW, 0.0056 mW, respectively. [76] demonstrated that ultrasonic systems achieved higher PTE and PDL than inductive schemes when the receiver is implanted deep inside the tissue of >10 mm. On the other hand, for bigger receiver dimension of 20 mm^3 and penetration depth of < 10 mm, PTE and PDL are higher for inductive links than ultrasonic ones [75]. Ultrasonic powering is therefore a promising approach for miniaturized implants at the mm-scale, large implantation depth (>5cm) while inductive powering is more suitable for larger implants with small implantation depth [77].

However, as concerns for adverse effects such as cavitation and temperature rise still exist, the spatial-peak temporal-average intensity (I_{SPTA}) must be < 720 mW/cm^2, spatial-peak pulse average intensity (I_{SPPA}) < 190 W/cm^2, mechanical index (MI) < 1.9, thermal index (TI) < 6 for diagnostic ultrasound as regulated by the FDA [78], [79]. A critical drawback of this approach is its high-attenuation rate in bones, which is a significant disadvantage for brain implants given the thickness of the skull. The ultrasound wave is attenuated at a rate of 13.3 dB/cm across 8 mm thick skull, of which 2.7dB/cm, 5.4 dB/cm is caused by longitudinal and shear absorption, respectively [80]. Impedance mismatch between the fabricated transducer and body tissues, which causes significant reflection of energy when ultrasound

encounters the body, poses another tough challenge that compromises the power transfer efficiency. To mitigate such effects, MEMS post-processing techniques, including metal deposition, etching, sputtering, and lithography, are required to append matching layers to the piezoelectric materials in both external and internal transducers [81], [82]. It is also a less ideal scheme for powering distributed neural implants as the piezo-crystals are particularly sensitive to depth and orientation misalignment [62].

C. INFRARED POWERING

The principle that infrared powering utilizes is very similar to that of EM and ultrasonic powering; light power is supplied through infrared lasers externally and the device located inside the body harvests such energy to power the implants. This approach utilizes the photovoltaic effect, a process in which electrons are ejected due to excitation by light and further results in the generation of electric currents [83]. As near-infrared (NIR) lights have the highest transmittance through skin tissues of around 20% among the infrared spectrum, wavelengths of 800nm to 1000nm is usually considered for this purpose [84].

To cater to the need of extending the lifetime of neural implants, batteries that can be recharged through photovoltaic cells have been studied and developed [85]. On top of specifically-designed optical chargers, ambient sunlight and infrared sources such as highly-prevalent surveillance systems can also be potential powering sources [86]. With laser exposure of 13 hours per week, the lifetime of the battery can be increased by 50%, which can further be increased with longer illumination time and higher intensity [44]. Another advantage of this scheme is its MRI compatibility, as the use of inherently MRI-incompatible components such as coils and antennas are obviated [87]. However, optical attenuation in tissues significantly compromises PTE as well as the penetration depth in this method [83]. Optical attenuation through tissues mainly results from absorption and scattering, and is a factor of the light wavelength, amounts of absorbing chromophores, and tissue type [88]. Although power conversion efficiencies of 17% for silicon photovoltaic (PV) cells and 31% for GaAs PV cells are achieved when the infrared irradiation is 1.06 μW/mm^2 at 850 nm, the efficiencies degenerate to around 3% and 6%, respectively, when the penetration through tissue (chicken breast) is 10 mm [86], [89]. The attenuation is more significant in skin tissues and skull: 92% and 80% of light in the NIR-I region (700 to 1000 nm) is attenuated through 1-mm thick skin and 0.9-mm thick skull (rat). Furthermore, after its propagation through 1-mm skin, 0.9-mm skull, and 1-mm brain tissues (rat), only 0.039% of the incident light remains [90]. Due to thicker brain structures in humans, even lower transmittance will be observed. Another disadvantage is the temperature dependence of photovoltaic cells. For every 1°C increase, PTE decreases by 0.097% for silicon PV and 0.069% for GaAs PV, which translates to approximately 0.97% and 0.69% lower
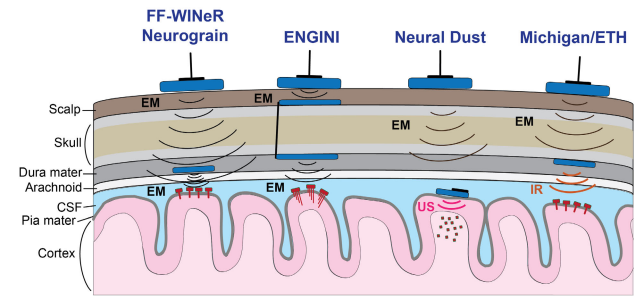

FIGURE 10. Various two-tier hybrid powering schemes.

PTE in human bodies when compared to the operation at 25 °C room temperature [86].

D. TWO-TIERED HYBRID POWERING

Although ultrasonic waves have been demonstrated to have higher power transmission efficiency than electromagnetic waves in soft tissues, ultrasonic waves do not transmit through bones efficiently. To properly utilize the peculiar characteristics of both electromagnetic and ultrasonic waves mentioned above, a two-tiered hybrid powering system, Neural Dust, has been proposed to optimize power transmission through the multi-layer structure of the brain [22], [34]. The system consists of three major components: the external transceiver placed close to the outer skin, sub-dural transceiver situated under the dura matter, and the neural implants distributed inside of the cortex. Electromagnetic wave is first propagated from the external transceiver through the skull to an intermediate transducer system in the sub-dural transceiver that converts electromagnetic to acoustic energy, which is then transmitted through soft tissues to power neural dust implants, as seen in the third system in Fig. 10. This system takes advantage of features of both EM and ultrasonic waves, so that power attenuation through both bone and soft tissues is minimized. The miniature scale (1-100 μm) of the motes combined with the one-to-multiple correspondence between the sub-dural transceiver and neural dust motes enable their extensive deployment throughout the brain, potentially leading to a significant increase in the number of neural recordings of various parts of the brain. However, when the size of the neural mote is decreased, the overall transfer efficiency of the power reduces as well. The measured PTE for the $127 \times 127 \times 127 \ \mu m^3$ neural dust mote is only 0.002064% [22]. Proper encapsulation of the extremely small piezoelectric transducers while exposing the two electrodes for neural signal recording remains a huge challenge. As more components are included in this design with the introduction of the intermediary transducer, the surgical complexity of inserting the whole system is increased. There is also the challenge of designing transducers that is small enough to fit below the dura, where extremely limited space is available. If these issues are resolved, this system is likely a reasonable option when either the implant is extremely small or the situate at a very deep location.

The two-tier system that utilizes near-field inductive coupling for both links is also proposed [91]. As shown in the first scheme of Fig. 10, the untethered neural probes in FF-WINeR and Neurograin systems are powered by a 3-coil inductive link, with an intermediate high-Q resonator placed underneath the dura matter that relays power and data between the external transmitter and implanted neural probes [92], [93]. The second system, ENGINI, in Fig. 10 depicts another powering scheme, which also utilizes inductive coupling for both links [94]. Its first tier includes an external primary coil that propagates energy transcutaneously to the secondary coils located above the skull, which are connected to the epidural coils below the skull through wires. These primary coils of the second tier are then inductively coupled with the free-floating implants scattered throughout the cortex. The advantage of the two designs mentioned above is two-fold: firstly, as the distance between the coupling coils is reduced significantly, the coupling coefficient is increased. The improvement in PTE is even more significant in the ENGINI system, as the transmission through the skull, the source of the greatest EM degradation, is obviated. Secondly, as power can be more uniformly distributed, the system becomes more robust and less vulnerable to positional and angular misalignment between the coils.

The last scheme in Fig. 10 illustrates another two-tier powering system that utilizes both EM and NIR means. The external device is inductively coupled with a repeater in the epidural space. The repeater receives the EM power from the external device, and powers and programs the microprobes placed in the sub-dural space via NIR light [38].

E. ENERGY HARVESTING

Numerous research groups have also looked into harvesting power from the ambient environment to sustain the energy needed for the operation of neural implants. Such energy harvesting systems typically utilize mechanical or chemical energy generated by the human body, which exempts the reliance on bulky internal energy-receiving and external energy-transmitting components.

One of the most common ways to harvest energy inside the human body is through extracting chemical energies of organic chemical pairs with high oxidation-reduction potential, also known as the biofuel cell. Among the many organic chemical pairs, glucose and oxygen are the most extensively used components due to their substantial quantity and general availability in the human body. The oxidation of glucose releases free electrons, during which electric current and therefore electric power is generated. This oxidation-reduction process is mediated by catalysts, which depending on their characteristics, determines the extend of glucose oxidation and thus, the amount of power generated [95]. A glucose fuel cell for neural implants potentially powered by the cerebrospinal fluid has demonstrated to produce 3.4 μW/cm^2 steady-state power [96]. Drawbacks of this method include the challenge of isolation, fixation, limited lifetime of the catalysts, and lack of long-term stability of the device [97].
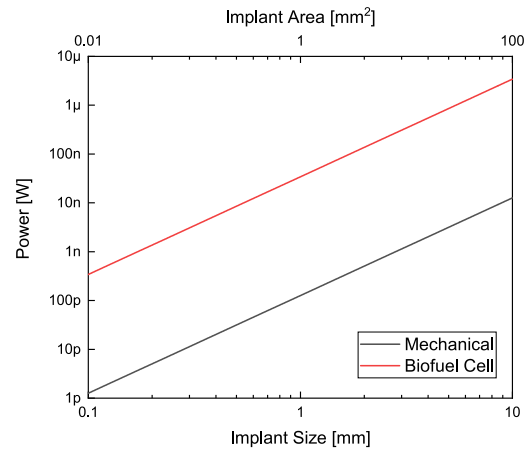

FIGURE 11. Power generated from mechanical and biofuel energy harvesting devices over the implant size.

Although the generation of power in the μW-scale might be just sufficient enough to power neural implants, the available power becomes too low when the size of the implant is decreased. As seen in Fig. 11, the power harvested from such system is only 34 and 0.34 nW when the area of the harvester is 1×1 and 0.1×0.1 mm^2, respectively.

Harvesting power from mechanical energy generated in the human body to power neural implants has also been vastly investigated, mostly through the application of piezoelectricity. When mechanical motions or vibrations are exerted, piezoelectric materials are capable of generating electric power, which is proportional to the strain being administered. The potential of collecting mechanical energy induced by pressure fluctuations in the cerebrospinal fluid (CSF) within the lateral ventricles is explored. Energy density of 12.6 nW/cm^2 was generated using such energy harvesting device (2.5 mm in diameter) and is possible to be increased up to 26 nW given the available space in the largest cavities of the ventricular system [98]. The very nature of the mechanism this approach utilizes, the need of space for motion or vibration, inadvertently renders it less efficient when it is scaled down. Power harvesting through the endocochlear potential (EP), an electrochemical gradient maintained by the inner ear, has been demonstrated *in vivo* to supply 1.12 nW from the ear of a guinea pig up to 5 hours [99]. However, the power extracted was very small, and was harvested and powered from in the ear, not the brain, which more stringent requirements should be fulfilled.

Although the concept of constructing a fully autonomous and self-sustained neural signal recording device appears attracting, the fact that minimal space is available near the brain area leads to the generation of power that is insufficient. The stochastic nature of most energy harvesting components also renders this approach unstable and unreliable.

III. CHALLENGES IN COMMUNICATION
Implantable neural interfaces need to communicate with the outside world to ensure a proper functioning of the implants

and to transmit recorded signals so that they can be monitored, processed, and utilized. Data transmission from the external device to the implant is called *downlink* or *forward* telemetry, and data transmission from the implant to the external device is called *uplink* or *backward* telemetry.

For neural recording implants, downlink data transmission is usually used to transmit configuration bits to the implant, which requires data transmission rate lower than 100 kb/s on a non-frequent, non-continuous basis, and therefore, poses less challenge and complexity. The most extensively used method is amplitude shift keying (ASK) [100] due to its simplicity, while other configurations such as frequency shift keying (FSK) [101] and phase shift keying (PSK) [102] are also applied. Forward telemetry is generally coupled and modulated with the power link, eliminating the need for a separate channel. This concept can be applied for both electromagnetic and ultrasonic waves, and therefore, is extensively utilized in communication systems for neural implants. For implants equipped with the function of stimulation, more information such as timing and magnitude of stimulation pulses should be delivered. However, the required data rate for downlinking stimulating signals is still much less than that for uplinking recorded signals. In [103], binary phase-shift keying (BPSK) modulation is used to achieve a maximum of 8 Mbps for uplink recorded data transmission while on-off keying (OOK) modulation is used to reach 100 kbps for downlink transmission. In [104], the full-duplex transceiver achieved 500 Mbps uplink data rate and 100 Mbps downlink data rate through either OOK or BPSK.

While there is less complexity associated with downlink data transmission, uplink data transmission poses a more profound challenge as less power and space are available on the implant side. The power restriction becomes a significant limiting factor as the size of the implant decreases. This is especially problematic for neural recording devices as an abundance of acquired signals need to be transmitted to external devices. Depending on whether the antenna needs to be driven actively or not, backward telemetry can be categorized into two types, either passive or active transmission.

One of the most widely used passive transmission is the backscattering approach, which can be utilized when operating over a short distance, such as when the external device is located directly on the head. Load shift keying (LSK) is one of the most extensively applied backscattering method, in which the power signal is modulated by shorting or opening the LC tank on the secondary side and then sent back to the external interrogator [105], [106]. As this method combines uplink data transmission with forward power delivery and only a switch is required to modulate the power carrier on the implant side, minimal power is needed to operate such scheme (few pJ/bit to tens of pJ/bit) [107]. However, as the original power supplied to the implant is transmitted the second time when uplinking data, there is significant attenuation of the signal. This results in an enormous magnitude difference between the strong power carrier signal and the weak uplinked signal, leading to a low modulation index and

rendering distinguishing the signals difficult [64]. This situation is particularly exacerbated when the size of the implant coil is decreased, which lowers the coupling coefficient (as in Fig. 6 (b)) and therefore further compromises signal clarity. To demonstrate the effect of implant size on the modulation index, a circuit model akin to Fig. 3 was constructed and simulations were conducted in Cadence. The R, L, C parameters for both transmitter and receiver coils were extracted from previously simulated HFSS models under optimal scenarios for each implant size. The modulation index is as high as 154% for implant size of 10 mm, yet drastically deteriorates to 0.157% for 1 mm (a 980-fold decrease), and further to 0.00005% for 0.01mm (another 3140-fold decrease), as illustrated in Fig. 12.
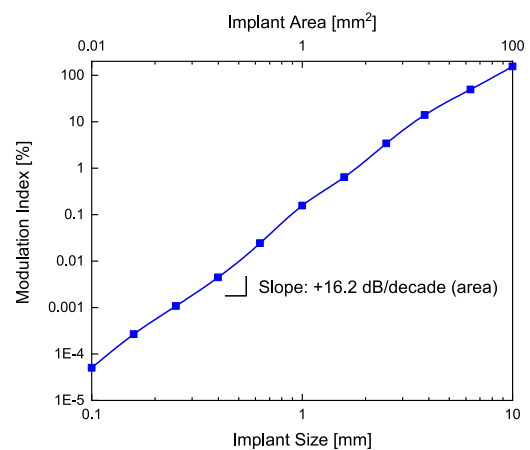
FIGURE 12. The relationship between modulation index and the size of the implant with a slope of 16.2 dB/decade in area.

Active transmission requires additional energy to actively drive the antenna and generate data carrier signals, and is usually applied when the transmission distance is longer, such as sending data from implants to mobile phones. Even though such far-field communication through electromagnetic radiation is well-developed and has been extensively applied [108], [109], it consumes several orders more energy (around 3 nJ/bit or more) than other components, such as the AFE (active front-end), ADC (analoge-to-digital converter), DSP (digital signal processing) of the implant (around tens of pJ/bit), making it a less desirable approach due to its high energy consumption [110]–[112].

To remedy the issues raised, an alternative candidate, impulse radio ultrawideband (IR-UWB) transmission, that can achieve high-data-rate, short-range, and low-power transmission has been explored [113]. This scheme is characterized by two unique features: (1) A short pulse of a few nanoseconds encoded with data is transmitted during the active period while remaining inert for the rest majority of the cycle [114]. (2) It does not involve sinusoidal carrier generation of high frequency signals. Both of these attributes lead to its low average energy consumption in the pJ/bit range. Also, as the range of the bandwidth utilized is large (3.1-10.6 GHz),

high data rates can be achieved [115]. For high rate systems, binary phase-shift keying (BPSK) is utilized and has demonstrated data rate of 100 Mb/s while pulse-position modulation (PPM) is applied for systems requiring lower rates and has achieved that of 16.7 Mb/s [116], [117]. In [118], a 60-GHz data transmission link of data rate 6 Gb/s, energy cost per bit of 2.08 pJ/b with low bit-error-rate of 10^{-12} at 6 mm transmission distance is achieved. Wireless neural interfacing system with transmitter based on asynchronous logic master–slave phase-locked loop (PLL) and receiver with non-coherent architectures achieved high data rate of 1 GHz with minimal power consumption of 17 pJ/bit while the area of the complete transceiver chipset is only 0.38 mm^2 [119], [120]. Furthermore, such system does not require the antenna to be large, which is conducive to shrinking the size of the implant coil [121].

However, as the system is dormant for the majority of the cycle, its peak transmission power is large in the active period. To support such substantial and instant current, a large capacitor that can store energy for a rather long time and supply a large amount of power instantaneously is needed. With the assumption that 833 mW in [122] is the power consumption of the transmitter that does not duty cycle, data transmission of 16.27 nJ/bit is achieved. Presume a single-channel neural recording system with required data rate of 100 kb/s (= 10 bit × 10 kS/s), the resulting duty-cycle ratio is 0.2%, indicating that the transmitter can be active for 0.2% and remain dormant 99.8% of the period to preserve energy. If the transmitter transmit every one second, 1.666 μJ of energy will be consumed and should be stored in the capacitor or energy storage device (the energy accounted here is merely for data transmission, more energy might be needed for initiating the transmission operation). This translates into the need of a 1 μF capacitor, which is, to date, not possible to be integrated in IC chips. While off-chip components are available, it is comparatively sizeable (0.6 × 0.3 mm^2) and therefore unfavorable when the ultimate goal is to decrease the size of the implant [123]. Furthermore, this approach operates at a rather high frequency of GHz to tens GHz range, which will lead to more energy absorption and therefore more signal attenuation in tissues [124].

IV. NEURAL SIGNAL RECORDING
Numerous neural information can be extrapolated from electrical signals recorded with neural implants. Although intracellular recording with microelectrodes produces strong and clear voltage signals ($\sim$ 70 mV_{pp}) [125], it typically induces death of the neuron due to the need of membrane penetration [126]. Also, the number of recording channels is not scalable and it requires very accurate and delicate instrumentation [127]. Hence, this approach can be more frequently seen in bench-top settings, while less applicable to high-channel-count mobile neural recording.

As a result, recording of both extracellular action potential (EAP) and local field potential (LFP), which is the average electrical activity of surrounding neurons, has been extensively utilized as they are less invasive and much more scalable than intracellular means. EAPs typically have signal amplitudes of approximately 50-500 μV_{pp} and frequency ranges of 0.8-10 kHz while amplitude of LFP is larger at around 0.5-5 mV_{pp} [126] and slower at a lower frequency range of 1-250 Hz. Major attention has been paid to action potentials of neurons, as they reveal a plethora of information regarding cell-to-cell communications and networks. EAPs also provide insights into the morphological and biophysical characteristics of the neuron [128], [129]. Even though most previous BCI researches were based on EAP recording, LFP recording has been indicated to be more suitable for chronic long-term monitoring [94]. The generation of scar tissues and induced foreign body response against the device implanted chronically result in the formation of a low-pass filter that obstructs the transmission of high frequency EAPs while poses less filtering effect for LFP [130], [131]. It has been demonstrated that LFP remains accessible over longer periods after implantation while EAP becomes incomprehensible [132]. However, as LFP is the average sum of multiple neural signal components, it is much more difficult to decode and identify the signal of the targeted neuron. On the other hand, EAP directly measures the signal of the targeted neuron, and has much higher temporal and spatial resolution than LFP [133].

Neural signal recording is achieved by measuring the potential difference between the readings of at least two electrodes. There are currently two major approaches in neural recording depending on how close the electrode pair is placed: *referential* and *differential* recordings. In *referential* recording (RR), an electrode is placed at the recording site of interest and another electrode in a reference area such as below the skull at the location right above the cerebellum. Electrodes for *differential* recording (DR) are positioned in close proximity at the to-be-inspected location. DR has been demonstrated both numerically and experimentally to be a more optimal approach for recording site-specific neural activities and is more favorable in miniaturized neural implants [134].

Volume conduction, the phenomenon of current flow by electrogenic cells and tissues, enables the possibility of detecting neural signals from afar as demonstrated in EEG and ECoG [135]. However, this same feature also inadvertently causes unwanted detection of activities in distant neural areas located between the recording and reference electrodes [136], [137]. This leads to significant interference and crosstalk, which are not conducive to the objective of recording the targeted local neural signal. The scheme of RR is particularly more vulnerable to such circumstance as the reference electrode is placed far apart and thus gravely subjected to serious crosstalk between the recording electrodes and interference from activities of neurons placed afar, while DR with a local return (or reference) electrode has been shown to minimize the impact of distal neural activities [134]. Furthermore, a distal ground cannot be implemented due to

the miniaturized geometry when the implant is scaled down to millimeter size.

In DR, the differential voltage V recorded across a pair of electrodes of a current source I of the targeted brain site can be expressed as

$$V(r_+, r_-) \cong \frac{I}{2\pi\sigma}\left(\frac{1}{r_+} - \frac{1}{r_-}\right) \qquad (6)$$

where σ is the volume conductivity of the neural tissue, and r_+, r_- are the distances from the targeted site to the electrodes, respectively. Here σ is assumed to be homogeneous. While the potential measured is inversely proportional to the linear distance between the electrodes and targeted neuron, it is still capable of reaching distance several times that of the electrode separation distance. According to simulation results, when the diameter of the electrodes is D and the separation distance is $2D$, the recording penetrable depth for single neural source is reported to be approximately $2D$ vertically and $4D$ horizontally [33].

As the size of the implant decreases, both the diameter of electrodes and their pitch will have to be reduced. One advantage of the implant miniaturization is that local neural sources can dominate more and be less subject to interference from distant sources because the electrode pair is closer in vicinity [134]. However, several challenging issues arise as a consequence of such miniaturization. Firstly, as the scale of implant decreases, the distance between the two recording points reduces, decreasing the absolute magnitude of the measured potentials. Even when the size of the electrodes are kept constant, merely reducing the distance of the two electrodes results in significant diminution of the measured peak-to-peak voltage. However, the pitch does not have to be infinitely increased to obtain the strongest recording, which saturates around spacing of 1.3 mm (electrode size: 0.2×0.2 mm) [138].

To investigate how the pitch of the electrode pair affects the magnitude of recorded neural signals while the electrode size remains unchanged, we conducted neural recording simulation in MATLAB through the model shown in Fig. 13 (a),(c) and Eq. (6). The size of the electrodes was kept constant of 0.2×0.2 mm and the pitch was swept from 0.3 to 1.8 mm with step size of 0.25 mm. The values used for the simulation include 0.47 S/m for the conductivity (σ) of the grey matter [139] and 50 nA for the current source (I) [140]. The current source (neuron) is placed directly below the center of one of the electrodes. It is observed that the recorded voltage increases with the increase of the pitch, but does not escalate indefinitely and saturates around 1.3-1.8 mm, which is in accordance with the findings in [138]. However, it is discovered that this only applies when the electrodes are placed in close proximity with the targeted neuron (0.1 mm), as seen in the black line in Fig. 14. When the electrode-neuron distance is larger, such as 1 mm as seen in the red line in the identical graph, the increase in the amplitude of the recorded voltage appears to be linear.
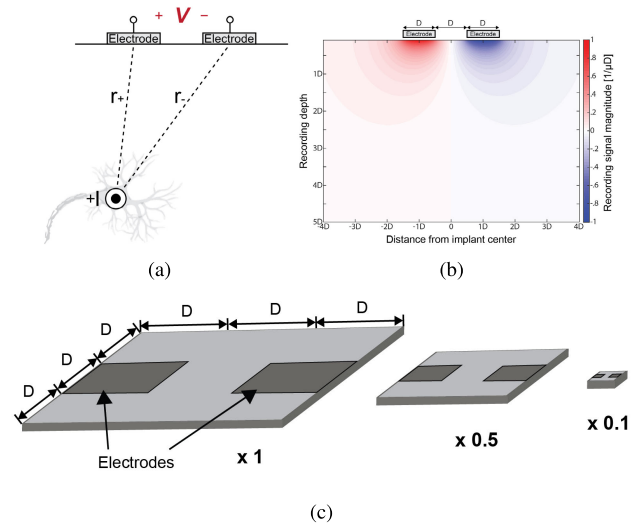

FIGURE 13. (a) The schematic of the differential recording approach: the two electrodes are placed in close proximity and interacts with the neural tissue (conductivity σ) below. (b) The spatial map of the effect the current source in the neural tissue has on the differential electrodes (represented in units of $1/\mu D$) [33] (c) The simulated implant model for neural recording and stimulation in MATLAB. The center and rightmost models represent the reduction in implant size by 50% and 90%, respectively.
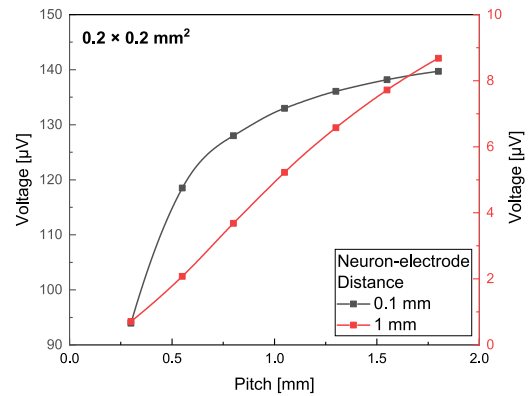

FIGURE 14. Simulation results of the relationship between the recorded voltage signal and the pitch while the electrode sizes remain unchanged at 0.2×0.2 mm². The black line is the relationship when the electrodes are placed in close proximity at 0.1 mm with the targeted neuron while that for the red line is larger at 1 mm.

Secondly, as the environmental, electronic and thermal noises still persist around the implant and does not scale down, the signal-to-noise ratio (SNR) is severely compromised [138]. This decrease in signal intensity necessitates the reduction of noise from the electronics, which inevitably needs to be achieved through supplying higher power [22]. The noise efficiency factor (NEF) illustrates this noise/power trade-off and is a widely used metric for describing the noise of a system, defined by the following equation:

$$NEF = V_{nrms,in} \times \sqrt{\frac{2I_{tot}}{\pi \times V_t \times 4kT \times BW}} \qquad (7)$$

where $V_{nrms,in}$ refers to the input-referred rms noise voltage, I_{tot} the total current drain, V_t the thermal voltage, and BW the amplifier's bandwidth in Hz [141]. Numerous methods have

been proposed to decrease NEF of the instrumentation ampli- fier (IA), while the lowest achieved NEF by far is approx- imately a bit below two [142]–[144]. For instance, using a current-reuse analog front-end (AFE) that includes a low- noise amplifier (LNA) and a programmable gain amplifier (PGA), NEF of 1.94 is achieved (3.2 μW $V_{rms,in}$) with mini- mal power consumed by the AFE (9 μW per channel) [145]. The trade-off between power, noise and implant size has been investigated in [138], with a conclusion of 50 μm as the smallest implant size that can obtain enough power to differentiate the signal from noise, assuming a SNR of 3 is required (for two-tiered Neural Dust system).

Thirdly, smaller electrodes have higher impedance, which results in a input signal degradation, and therefore the AFE requires corresponding higher input impedance so that the clarity of sensing will not be compromised [146]. Impedance boosting techniques that have been employed to address this issue include canceling parasitic capacitance through tech- niques such as active shielding [147], [148] and negative capacitance [149], [150].

To ascertain how implant size affects the magnitude of recorded neural signals, we simulated implant sizes from 0.1×0.1 to 10×10 mm in MATLAB with identical settings delineated previously. Each implant has two electrodes one third the length of the implant and are configured farthest apart from each other to maximize the pitch and electrode area, while peripheral space for the coil inductor is not consid- ered in this case. The reduction in pitch of the electrode pair is in proportion to the decrease in the size of the electrodes, as seen in Fig. 13 (c), which shows the schemes when the implant size is reduced by 50% (center) and 90% (right). Rather than the expected straightforward result of "bigger implant, stronger signal", it is observed that the maximum magnitude of the recorded voltage depends significantly on the depth measured. At smaller electrode-neuron distance of 10 μm shown in Fig. 15 (a), the implant of the smallest size (0.1×0.1 mm^2) has the maximum voltage magnitude. At deeper distances of 50 μm and 0.5 mm, implants of medium sizes (0.4×0.4 mm^2 and 4×4 mm^2, respectively) have the maximum recorded voltage. At even larger distance of 1 mm, a bigger implant size of 6.3×6.3 mm^2 appears to perform the best as seen in Fig. 15 (d). It is observed that smaller implants have better focusing effect for the recording of nearby local sources. It also shows that the optimal size of the electrodes to be utilized depends on the depth of the targeted neuron. In other words, when the neuron is close-by, it is more efficient to use electrodes of smaller pitch. On the other hand, it is more desirable to use those with larger pitch when the tar- geted to-be-simulated neuron is farther away. The black dots in Fig. 15 (e) show the implant size of which the strongest sig- nals can be acquired for various recording depths. It appears that the most desirable and efficient recording electrode size is a factor that should be optimized based on the neuron- electrode distance. Although this phenomenon has not been addressed much in the field, it has been explored and high- lighted in some studies previously. [134] calls attention to the
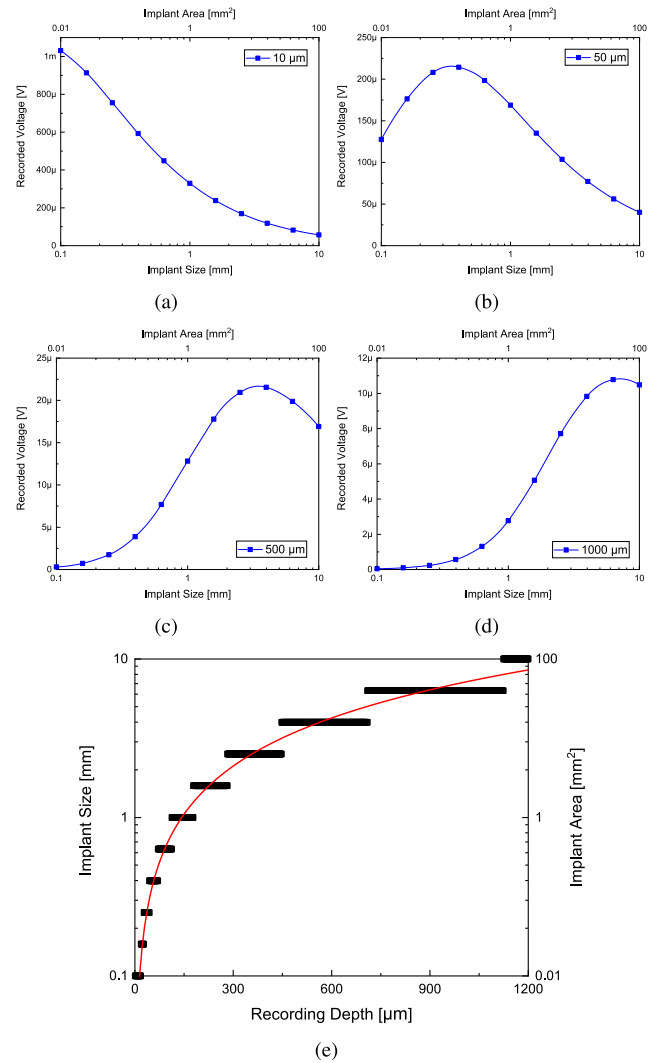

FIGURE 15. Simulation of recorded voltage amplitude with varying implant sizes ranging from 0.1 to 10 mm for various electrode-neuron distance: (a) 10 μm, (b) 50 μm, (c) 500 μm, and (d) 1000 μm. (e) The optimal implant sizes for neural recording for electrode-neuron distances from 0 to 1200 μm. The black dots are the simulation results while the red curve is a trend-line fitted with a Allometric1 function in OriginLab.

observation that the closer the two electrodes forming a pair, the more visible the local source. It has also been demon- strated both experimentally and computationally that when the neuron-electrode distance is minimal (1-100 μm), smaller electrode size actually leads to higher recorded voltage and signal-to-noise ratio [151]. For more in depth analysis on the optimal electrode size for neural potential recording, readers can refer to [151]. Another observation worth highlighting is the drastic attenuation of recorded voltage for deeper neurons. Voltage signals recorded are around the range of 100s μV and 1 mV while that quickly decreases to few μV for recording depth at 1 mm. [152] has reported similar observations: while 400 μV was recorded at a distance of 20 μm, it drastically dropped to 50 μV at only 60 μm away from the electrode (a 9.03 dB decrease).
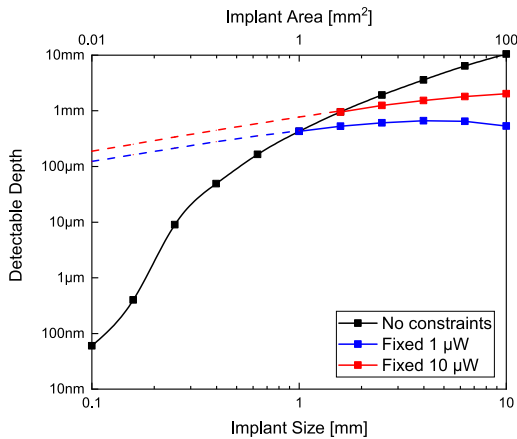
FIGURE 16. Simulation results of the detectable depth of neural signal recording for various implant sizes. The solid blue and red lines represent results with AFE power constraints; the maximum power that can be consumed by the AFE was set to 1 μW and 10 μW, respectively. The dotted lines represent the results when the power AFE consumes is at constant values of 1 μW and 10 μW across all sizes. The black line represents the penetration depth with no such constraints.

To investigate how the detectable depth for neural signal recording is affected by the implant size, the factors of power and noise need to be considered. Using the maximum PDL obtained through previous simulations in Sec. II, with the assumptions that 50% of power received by the implant to be consumed by the analog front-end (AFE), V_{DD} to be at constant 1 V, and NEF to be at the theoretical limit of 2.02 [153], the achievable minimum input-referred noise for each implant size can be calculated. The bandwidth was set to 10 kHz for neural spike detection [154], temperature to the body temperature 310 K, and load resistance to 1 MΩ. As a model of firing neuron, a current source of magnitude 50 nA was placed at the center below of one of the electrodes [140]. To ensure that the recorded signal can be distinguished from noise, the detection threshold is set as three times of the input-referred noise. Fig. 16 shows detectable depths of neural spikes over the implant size. The black line in the figure shows that signal sources up to 10.5 mm deep can be detected by an implant with size of 10 $\times$ 10 mm^2, 0.427 mm at 1 $\times$ 1 mm^2, while that significantly decreases to 60 nm at 0.1 $\times$ 0.1 mm^2. Although the maximum transmittable power rises with the increase in implant size, it is not practical to assume that the power AFE consumes will increase indefinitely. Therefore, a limit on the power consumption of AFE was introduced, and its resulting detectable depths were calculated. The blue line in the figure represents the scenario with the 1 μW constraint while the red one illustrates that for 10 μW. The dotted lines represent the cases when these fixed amounts of power (constant 1 μW and 10 μW) were available for the AFE. As the power delivered to AFE remains constant in this scenario, the decrease in the detectable depth is resulted from the reduction in the pitch and dimension of the electrodes. An even more drastic decrease in the detectable depth was observed when the maximum achievable PDL were taken into account for various implant sizes. The PDL is

comparatively smaller for implants of miniature sizes, and therefore, their reachable depths are correspondingly smaller. The sizable gap between the dotted and solid lines is the consequence of the reduction in power transmitted to the implant.

V. NEURAL STIMULATION

Electrical stimulation of targeted brain regions has been demonstrated to be effective treatments for numerous disorders [24], and has further been applied to facilitate pain management [155], restore vision through visual prostheses [156], reestablish motor control [157], moderate emotion state [158], etc. Such therapies provide an alternative, less invasive option so that more extreme treatments such as hemispherectomy (removal or disconnection of half of the brain) or lobotomy (severing connections in the prefrontal cortex) can be obviated [159], [160]. As those in need of neural stimulation therapies usually already have cortical implants for monitoring purposes, the identical configuration can be utilized for stimulation, and therefore no extra invasive procedure is needed. To accurately determine the timing and intensity of the stimulation so that individual needs can be catered, an autonomous closed-loop electrical control platform that synchronizes the recording and stimulating systems is needed [161], [162].

Several challenges associated with smaller form factor and higher channel density of neural stimulating devices persist. Firstly, decreasing the size of stimulating implants necessitates the miniaturization of electrodes, and inevitably, increased impedance of the electrodes [10], [163] and decreased coupling capacitance [164]. The total deliverable charge per phase of stimulation Q_{ph} can be expressed as

$$Q_{ph} \cong I_{stm} \cdot T_{ph} = C_{el} \cdot V_{range} \qquad (8)$$

where I_{stm} is the stimulation current, T_{ph} is the duration of each stimulation phase, C_{el} is the coupling capacitance of electrode, V_{range} is the total stimulation voltage excursion. As the coupling capacitance decreases, higher voltage must be applied to achieve the same intensity of stimulation. For instance, a Pt black microelectrode of a geometric area 1000 μm^2 (31.6 $\times$ 31.6 μm^2) has a coupling capacitance of 0.545 nF [165]. To achieve 10 nC per phase in stimulation, which is close to the minimum charge to initiate neural activation, the voltage of at least 18.3 V is needed in the stimulator. This further leads to issues of higher power consumption, system complexity, and challenges of generating and handling higher voltage.

Potential solutions to improve the performance of the electrodes surround the notion of reducing their impedance. This can be achieved by developing new materials such as carbon nanotube (CNT) yarn, which has attracted great interests as it demonstrates great electrical conductivity, mechanical strength, flexibility, and biocompatibility [166]. CNT yarns have been shown to be ten times more conductive and flexible in comparison to platinum iridium wires, which can significantly reduce recording noise and decrease the harm on
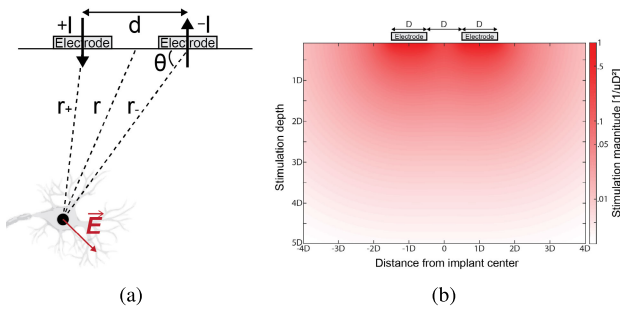
FIGURE 17. (a) The schematic of the differential stimulation approach: the two electrodes are placed in close proximity and interacts with the neural tissue (conductivity σ) below. (b) The spatial map of the effect when the stimulating current has on the cortical tissues (represented in units of $1/\mu D^2$) [33].

tissues due to rigidity [167]. Even after the insulation coating of Parylene-C, the increase in impedance of the CNT electrode is minimal from 0.44 to 0.47 kΩ (diameter 40 μm at 1k frequency) [168], [169]. CNT yarns have also exhibited large charge storage capacity of 12.3 mC/cm^2, which is higher than that of Pt–Ir electrodes (5 mC/cm^2), and can further be increased to up to 98.6 mC/cm^2 with acid treatments [170].

Another approach seeks to increase the effective surface area through modifying the 3D structure or performing post-processing surface treatments such as electrodeposition [171], [172]. Intrinsically conductive polymer poly(3,4-ethylenedioxythiophene) polystyrene sulfonate (PEDOT-PSS) has been extensively utilized as coating of electrodes due to its high charge capacity and low impedance, which has been shown to decrease the impedance of the electrode up to 10-fold [173], [174]. It has also been demonstrated to have high flexibility and biocompatibility, enabling it to be applied *in vivo* [175]–[177].

Secondly, shrinking the pitch of an electrode pair intrinsically decreases the electric field generated by differential stimulation currents. Differential stimulation consists of two electrodes placed in close proximity, which interact with the tissues located below through supplying stimulating currents. The schematic of neural stimulation can be seen in Fig. 17 (a) and the resulting spatial map of the stimulating effect is shown in Fig. 17 (b). The electric field $\vec{E}$ induced by differential stimulation through the two electrodes can be expressed as

$$\vec{E}(r_+, r_-) \cong \frac{I_{stm}}{2\pi\sigma}\left(\frac{\vec{u}_{r_+}}{r_+^2} - \frac{\vec{u}_{r_-}}{r_-^2}\right) \qquad (9)$$

where $\vec{u}_{r_+}$ and $\vec{u}_{r_-}$ are the radial vector of the current flow direction, d is the pitch of the electrode pair, I_{stm} is the current flowing through the electrodes, σ is the medium conductivity, and r is the distance from the targeted neural site to the midpoint of the electrode pairs, while r_+ and r_- are the distances from targeted site to the electrodes. With the assumption that $r_+, r_- \gg d$ ($r_+^2 r_-^2 \cong r^4$, $r_+^2 + r_-^2 \cong 2r$), the magnitude of electric field can be expressed as follows:

$$|\vec{E}| \cong \frac{I_{stm}}{2\pi\sigma}\frac{2(r_- - r_+)}{r^2} = \frac{I_{stm}}{2\pi\sigma}\frac{2d\cos\theta}{r^2}. \qquad (10)$$

It can be discerned that the electrode pitch is proportional to the electric field generated. Thus, as the pitch is decreased, more current is needed to achieve the identical intensity of stimulation, which implies the need for more power and higher voltage range V_{range} in Eq. (8).

To discern how the magnitude of the electric stimulation is affected by implant size, we once again conducted neural stimulation simulation in MATLAB through the model shown in Fig. 17 and Eq. (9). As before, we simulated implant sizes from 0.1×0.1 to 10×10 mm^2 with the presumption that each implant has two electrodes one third the length of the implant and are configured farthest apart from each other to maximize the pitch. The values used for the simulation include 0.47 S/m for the conductivity (σ) of the grey matter [139] and 100 μA for the stimulation current I_{stm} [178].

Akin to simulations results in Sec. IV, it is observed that the maximum magnitude of the induced electric field depends significantly on the depth measured. At smaller electrode-neuron distance, such as at depth 50 μm as seen in Fig. 18 (a), the implant of smaller size (0.16×0.16 mm^2) has the maximum electric field strength. At slightly deeper distance of 300 μm and 1 mm, implants of medium sizes (1×1 mm^2 and 2.5×2.5 mm^2, respectively) have the maximum electric field strength. At even larger distance of 3 mm, a bigger implant size of 10×10 mm^2 appears to perform the best as seen in Fig. 18 (d). It is once again observed that small implants have better focusing effects and is better suited at stimulating close-by or local neurons. As seen in Fig. 18 (e), it seems that the most desirable and efficient stimulating electrode size is a factor that should be optimized based on the neuron-electrode distance. One of the issues here is that although the electrode-neuron distance is a significant determining factor, it varies a lot depending on the depth and location of the neuron and implant and is difficult to control and measure in real applications.

Although the threshold of stimulation is a factor of the cortical neuron morphology, cortical cell type, amplitude/frequency of stimulating current, orientation, etc. [179]–[181], it is generally around the range from 0.1 to 1 V/m [182]–[184]. With the assumption that 0.8 V/m is required to activate a neuron [185], the relationship between penetrable depth and implant size is obtained in Fig. 19. Stimulation of neurons up to 5.64 mm apart can be achieved at 10×10 mm^2 while that reduces to 1.38 mm at 0.1×0.1 mm^2. The simulation result is in accordance with what we have expected: the smaller the implant size, the shorter the penetration depth.

An alternative method to the currently extensively investigated electrical stimulation is optogenetics, an approach that utilizes light to control the behavior of cells, neurons in particular [186]. This method requires genetic engineering of the targeted neuron to express light-sensitive channel proteins in the membrane, which is achieved by infecting the neuron by viral agents having genes that encode for the particular protein [187]. The action potential in the targeted neuron can be altered directly through either turning on or off the
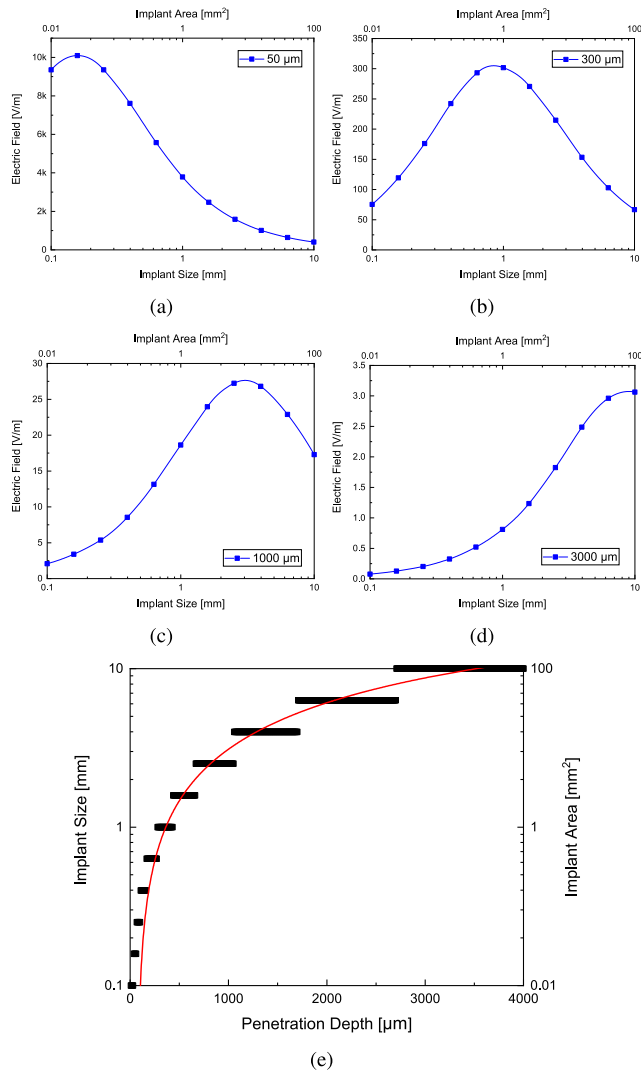
FIGURE 18. Simulation results of the relationship between the electric field magnitude and implant size for various electrode-neuron distance: (a) 50 μm, (b) 300 μm, (c) 1000 μm, and (d) 3000 μm. (e) The optimal implant sizes for neural stimulation for electrode-neuron distances from 0 to 4000 μm. The black dots are the simulation results while the red curve is a trend-line fitted with a two-phase exponential association equation.

FIGURE 19. The penetration depth of neural stimulation for implant sizes from 0.1 to 10 mm under the assumption that 0.8 V/m is required to activate a neuron.

Mini-LEDs with chip sizes ranging from 100 to 200 μm are currently commercially available [190]. To reach even smaller sizes, $30 \times 30 \ \mu m^2$ GaN μLEDs [191] and $10 \times 15 \ \mu m^2$ InGaN μLEDs that can be integrated on silicon neural probes have been developed [192], [193]. Secondly, high light attenuation through both absorption and scattering in multi-layer cortical tissues precludes the light from reaching deeper regions in the brain (wavelengths of 405-680 nm are generally used for optogenetcis). The propagation depth of μLED of 30 μm diameter through brain tissues is $\approx$ 200 μm for input current of 0.25 mA and $\approx$ 600 μm for that of 4 mA [194]. To expand its penetrable depth, approaches of either increasing light intensity or the number of μLEDs should be employed, yet this inevitably poses higher risks of tissue heating, which should not exceed the 2K regulatory limit [195]. However, with appropriately chosen illumination designs and conditions, heating can be minimized as low as 0.35K for single-cell activation [196]. Also, intricate devices such as wave-guides might be needed to deliver light beyond the superficial proximity of the light source. Another major challenge is its bio-compatibility and stability for long-term implantation. Furthermore, as genetic modification of the targeted neuron is required, the applicability on living human cells and its potential health repercussions is still unclear and debatable. Currently, employments of optogenetics are restricted to animal models and other applications such as facilitating drug tests [197].

The need for higher energy than electrical neural stimulation and therefore lower efficiency is another downside of optogenetic stimulation in implants. This translates to the need of including energy storage devices (capacitors or batteries) that are more sizable, which is not conducive to scaling down of such devices. To compare the efficacy of the two stimulation schemes, the maximum achievable stimulation frequencies were calculated. For optogenetic stimulation, with the assumption that 3.3 V and 20 mA were supplied to the stimulating LEDs [198], [199] and 10 ms is

light source [188]. As the channel protein has its particular activation spectrum, only the neuron with its addition will be effected, and therefore significantly increases the specificity of the stimulation. This method also enables inhibition of neural activities on top of excitation, while electrical stimulation can only achieve the latter [189]. Furthermore, since no electrodes are needed for this approach, the various challenges delineated regarding electrodes previously is no longer a concern.

However, this method comes with its own series of challenges. Firstly, a light source such as light emitting diodes (LED) or laser diodes (LD) needs to be added. To exempt the need of connecting wires or waveguides, a light source that can be integrated to the neural implant is desirable, which translates to the need of its miniaturization.
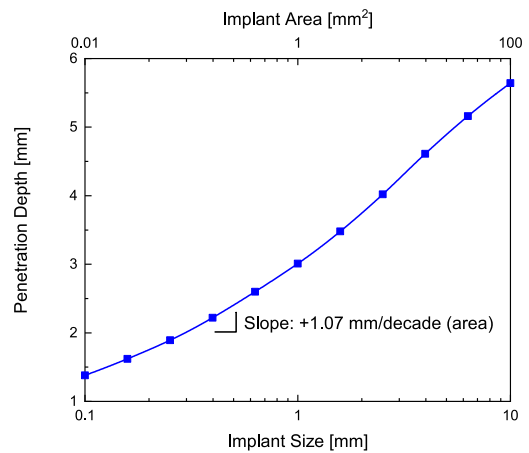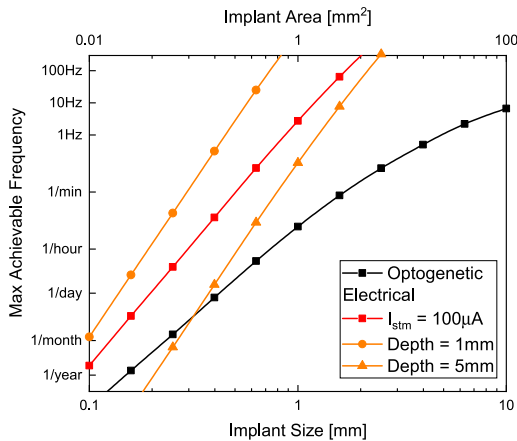
FIGURE 20. The maximum achievable stimulation frequency of optogenetic and electrical stimulation for various implant sizes. The red line represents electrical stimulation with constant 100 μA stimulation current while the orange lines represent the results with specific stimulation depths across the sizes of interest.

the pulse width necessary to achieve a full response [200], the power needed is calculated to be 600 μJ per stimulation. For electrical stimulation, the impedance of Pt electrodes of various sizes are inferred from the theoretical interface capacitance 0.545 F/m^2 reported in [165]. With 100 μA as the stimulation current [178] and 1 ms as the pulse width, the driving voltage (calculated with Eq. (8)) and power required are obtained for each implant size. Using previously obtained max PDL for various implant sizes in Sec. II and factoring in the 50% power for PMU, the powers available for stimulation are acquired and and their maximum achievable stimulation frequencies are plotted as seen in the black and red lines in Fig. 20. According to simulation results, electrical stimulation can achieve higher frequencies than the optogenetic approach. For implant size of 10 $\times$ 10 mm^2, >100 Hz and 6.69 Hz can be achieved for electrical and optogentic stimulation, respectively, while those are 2.75 Hz and 0.0014 Hz for 1 $\times$ 1 mm^2. This aligns with simulation results in [201], which shows that the maximum mean spike frequency (MSF) is higher for electrical stimulation (230 HZ at I = 1 A/m^2) than that for optogenetic stimulation (95 Hz at I = 1000 W/m^2). However, the achievable frequencies for both stimulation schemes reduce to less than twice a year for implant size of 0.1 $\times$ 0.1 mm^2, which is too low to be applied practically.

Further analysis was conducted to discern how targeted depth affects the achievable frequency of electrical stimulation. The required I_{stm} is obtained through simulations in MATLAB for the depths of interest with the 0.8 V/m threshold [185]. The required stimulation power and achievable frequency are then obtained as previously described. The maximum achievable frequencies for stimulation at depths 1 mm and 5 mm can also be seen from the orange lines in Fig. 20. The maximum frequency is lower for stimulation of deeper depth, as more power is needed.

VI. SYSTEM EXAMPLES (STATE OF THE ART)

Numerous millimeter-scale implantable neural interfacing systems have been developed, which are targeted to be applied to either the central or peripheral nervous systems for both clinical and research purposes. These systems are equipped with either of or both neural recording and stimulating functionalities. As the implants are scaled down to the millimeter size, they can be distributed more extensively throughout the region of interest. The free-floating and untethered scheme also minimizes the potential for infection and serious tissue response. In lieu of bulky batteries, wireless powering is utilized in all cases, with electromagnetic waves being the most preferably applied [205]. The interfacing system typically includes two modules: an internal implanted component for recording or stimulating the targeted part of the brain, and an external wearable component for powering and data acquisition. On top of the two components, in several cases, an additional coil or component is introduced to the system, which serve as the intermediary that increases the efficiency of wireless power and data transmission [92]–[94]. Current state-of-the-art millimeter-scale free-floating implantable neural systems are shown in Fig. 21, and their performance and functionality are summarized and compared in Table. 1. One of the potential challenges of the free-floating scheme is movement of the free-floating implants. To address this issue, techniques to fixate free-floating probes in or on the target brain tissues should be further developed. Another aspect is to reduce neural probe rigidity so that stress and tissue response at the interface can be minimized. Recording and stimulating electrodes developed to this end include the nanoelectronic thread (NET) electrodes (Luan *et al.*, *Science Advances*, 2017), neural ribbon electrode (Xiang *et al.*, *Advanced Materials*, 2016), and split ring electrodes (Lee *et al.*, *Sensor Actuat B-Chem*, 2017). As there is still a plethora of challenges that needs to be overcome, all millimeter-scale neural implantable interface systems are currently still in the research stage.

Several millimeter-scale BCI systems have been developed to target for neural recording [92]–[94], [202]. As expounded earlier in Sec. II-D, the Neural Dust recording system consists of three major components (external transceiver, subdural transceiver, neural dust mote) and utilizes both EM and ultrasonic waves for power and data transmission [22]. Its downlink ultrasonic transmission includes delivering power and the configuration signal to the implant, while the uplink transmission backscatters the signals modulated by electrophysiological signals. The single-channel dust mote of 2.4-mm^3 volume is composed of an application-specific integrated circuit (ASIC) chip, piezoelectric crystal, custom transistor, pair of recording electrodes, and assembled on a flexible PCB. A medical grade UV-curable epoxy is used to encapsulate the whole dust mote to provide insulation. Experimental *in vivo* validation on the PNS and skeletal muscles of rats was conducted, yielding high-fidelity electromyogram (EMG) and electroneurogram (ENG) signal recording results [202]. The size of the transducer, piezoelectric crystal
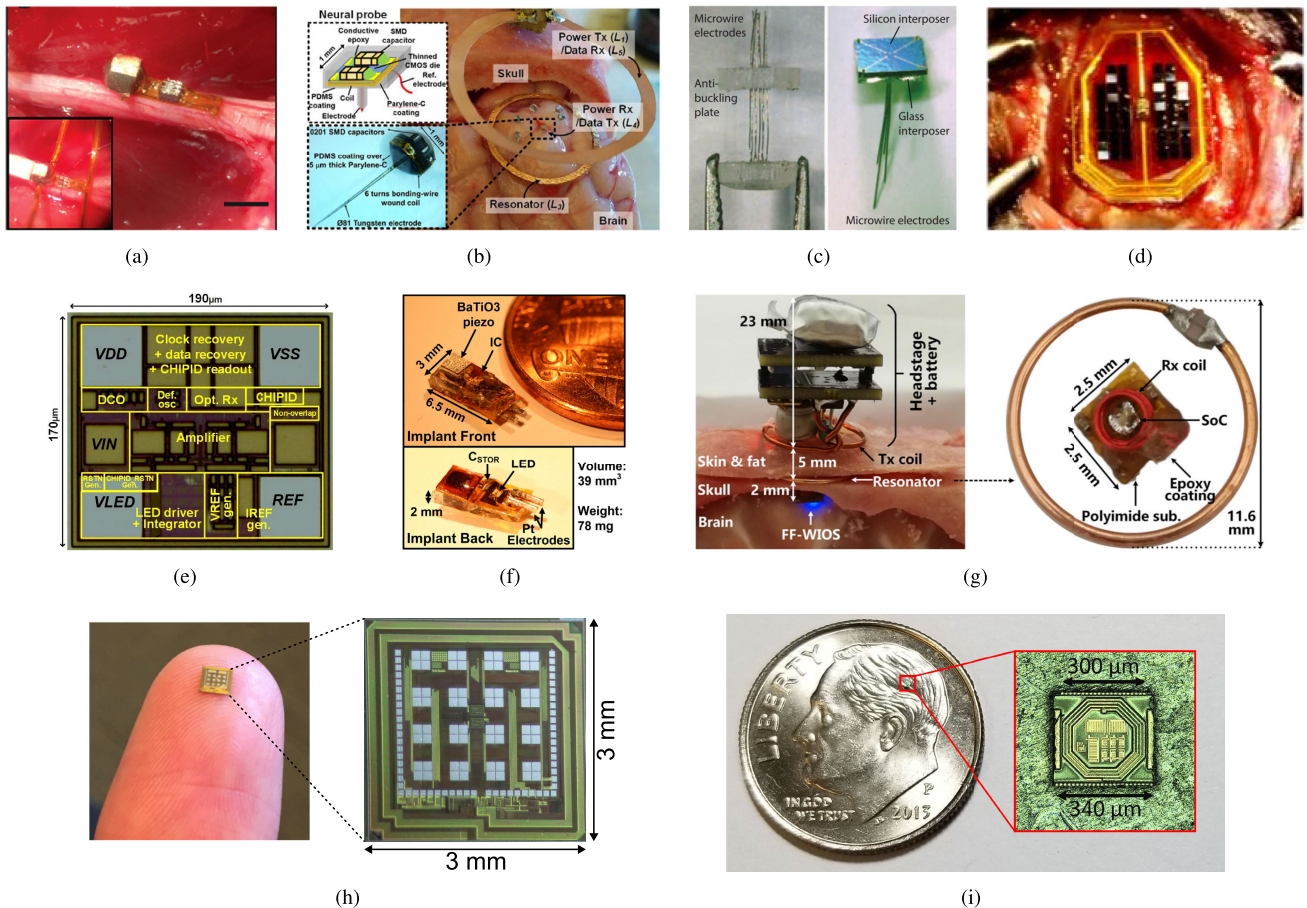
FIGURE 21. State-of-the-art free-floating millimeter-scale implantable neural interfaces: (a) Neural Dust [202], (b) Free-Floating Wireless Implantable Neural Recording (FF-WINeR) System-on-Chip (SoC) [92], (c) Empowering Next Generation Implantable Neural Interfaces (ENGINI) [94], (d) Neurograin [93], (e) Combined EM/IR recording system developed by University of Michigen and ETH Zurich [38] (f) The combined electrical/optical stimulator [203], (g) Free-Floating, Wirelessly powered, Implantable Optical Stimulation (FF-WIOS) device for untethered optogenetic neuromodulation [204], (h) Encapsulated neural interfacing and acquisition chip (ENIAC) [33], (i) Microbead [37].

and the size added by assembly and packaging processes remain major constraints for its minimization. The SNR of the back-scattering link is the principal limitation for shrinking the piezoelectric crystal in the mote, which can potentially be improved by increasing the dust mote's sensitivity and external transceiver's noise performance. Micro-fabrication techniques can be employed to improve feature size resolution. Another challenge facing the Neural Dust motes is the lack of long-term, reliable hermetic packaging. Piezoelectric materials in the motes typically have low Curie temperatures, rendering conventional hermetic sealing techniques unfeasible [202].

Free-Floating Wireless Implantable Neural Recording (FF-WINeR) System-on-a-Chip (SoC) of 1.1-mm^2 size has been developed [206]. The small, untethered neural recording probes are powered by 3-coil inductive link, with an intermediate high-Q resonator placed underneath the dura matter that relays power and data between the external transmitter and implanted neural probes. The FF-WINeR ASIC consumes minimal power of < 0.3 mW and includes sub-units such as the analog front-end (AFE), power management unit (PMU), active back telemetry (ABT), etc.

Recorded activities through the probes are first amplified with a low noise amplifier (LNA) of 35-dB gain, filtered with a 0.1-12 kHz band, digitized by a 10-bit analog-to-digital converter, and then transmitted through active back telemetry with 800 kbps data rate to the external data receiver. On top of the 3-coil inductive link used for powering, an additional coil is added for data transmission [92]. Akin to other wireless EM transmission systems, one of the major challenges of FF-WINeR is the trade-off among the implant lifetime, PTE, PDL constrained by SAR, and implant size. Although smaller implant size minimizes the formation of scars and thus increases the lifespan of an implant, active circuit area and the PTE/PDL of the inductive link are reduced. The extreme small size of the FF-WINeR probes also requires a novel process flow for its production that includes micro-machining, micro-assembly, and hermetic packaging, which is elaborated in detail in [65]. Though the *around*-CMOS coil achieves high *Q*-factor, it is subjected to higher variability in its electrical properties, which could be improved by employing a high-end fully automated wire-bonding process [62].

Empowering Next Generation Implantable Neural Interface (ENGINI) features three components: the external

TABLE 1. Comparison of State-of-the-Art millimeter-scale free-floating implantable neural interfaces.

		Recording					Stimulation		Both	
		Neural Dust [202]	FF-WINeR [92]	ENGINI [94]	Neurogram [93]	Michigan/ETH [38]	Stanford [203]	FF-WIOS [204]	ENIAC [33]	Microbead [37]
General	Neural Implant Volume [mm³]	2.4	<1	12.56	0.00675	~0.00323	39	9.4 (*in vitro*) 224 (*in vivo*)	2.25	0.009
	IC Area [mm²]	-	1.1	2.1	0.25	0.0323	3.58	1.1	9	*NA*
	Extra components implanted	Sub-dural Transceiver	High-Q resonator	Cranial Transponder	Relay Coil	Repeater	None	High-Q resonator	None	None
	Number of channels	1	1	8	1	1	4	16	16	1
	Technology [µm]	-	0.35	0.35	0.065	0.18	0.18 HV	0.35	0.18 SOI	0.13
	Power Supply [V]	*NA*	1.8	1.5	0.6	1.5	1.8	1.8	0.8	1
	Total Power Consumption [mW]	0.12	<0.3	0.092	0.04	0.00074	3	1	<0.1	*NA*
	Testing	*in vivo*	*in vitro*	-	*in vivo, ex vivo*	*in vivo*	*in vitro*	*in vitro, in vivo*	-	*In vivo*
Powering	Scheme	EM/US	EM/EM	EM/EM	EM/EM	EM/IR	US	EM/EM	EM	EM
	Frequency [Hz]	1.85M	131M	433M	1G	850nm+	1.314M	60M	190M	1.18G
	Rx Coil size [mm²]	0.56*	1.21	12.25	0.25	0.01615#	2.7*	10.2	9	0.09
	Number of coils	-	4	3	3	-	-	3	2	2
Communication (Forward/ Backward)	Scheme	- /NA	- /IR-UWB	- /LSK	ASK-PWM/BPSK	PWM/SIM	PWM-ASK/ -	OOK/LSK	ASK/LSK	*NA*
	Frequency [Hz]	- /1.85M	- /131M	- /433M	1G/1G	-/NA	1.314MHz/ -	60M/60M	190M/190M	*NA*
	Data Rate [b/s]	- /0.5M	- /0.8M	- /205k	1M/10M	-/NA	11k/ -	50k/160	*NA*	*NA*
Recording	Input noise [µV]	180	3.78	1.8	2.2	4.8	*NA*	*NA*	2.5	*NA*
	NEF	*NA*	2.16	*NA*	*NA*	3.76	*NA*	*NA*	4	*NA*
	ADC Resolution [bits]	8	10	12	8	*NA*	8 (DAC)	-	10	*NA*
Stimulation	Max current [µA]	-	-	-	-	-	5000	-	145	46
	Max light intensity [mW/mm²]	-	-	-	-	-	23	10	-	-
Notes		Utilize both EM and US.	Separated power and data coils	-	-	Utilize both EM and IR.	Combine both optical and electrical stimulation	Optical stimulation	Antenna integrated on chip	Antenna integrated on chip

*: lateral dimension of the piezo.   +: wavelength of IR light   #: area of PV cell   -: not applicable   *NA*: not mentioned in the study

processor, cranial transponder (anchored to the skull), and intracortical probes that are powered through inductive coupling at 433 MHz [94]. The probe is composed of two independently-developed modules, the active silicon head and the passive interposer that contains the electrode array, which are connected through solder bonding. Each probe has eight electrodes (array of niobium microwires) that can be used to record local field potentials (LFPs) at different depths. Adaptive referencing is employed at each probe to increase the spatial focus of LFP signals. Although the probe microwire electrodes are flexible enough to mitigate undesirable tissue response, its flexibility renders the insertion more challenging. A robotic surgical insertion device and anti-buckling probe structure have been developed to streamline the probe insertion process and prevent the delicate microwires from bending [94].

Neurogram of 0.00675-mm³ volume with a 0.25 mm² ASIC chip has been developed for neural signal recording [93]. Each Neurogram consumes 40 μW and serve as an individual sensor node, which can be widely distributed to form a cortical neural recording network. Both powering and telemetry are achieved through a near-field 3-coil wireless link at 1 GHz. Its uplink data transmission is achieved through RF backscattering with 10-Mbps data rate. Each chiplet features a unique on-chip ID, which can be used to queue the nodes for the TDMA communication network. Each sensing node is hermetically encapsulated with ALD-based stacked multilayer conformal coatings, which was tested to remain viable for over 10 years [93]. Currently, research on Neurogram focuses on integrating the sensing and stimulation modules on the single chiplet and developing bidirectional synchronized TDMA network.

As described earlier in Sec. II-D, the neural recording system developed jointly by University of Michigan and ETH Zurich consists of three major components (external interrogator, the epidural repeater, micro-probes) and utilizes both EM and NIR waves for power and data transmission. The neural recording probe includes a carbon fiber electrode that penetrates several millimeters into brain tissues. The IC of the probe is of dimension 0.19×0.17^2 and consumes minimal power of 0.74 μA. It features on-chip computing of neural spike band power, maintaining accurate finger position and velocity decoding with minimal power consumption. The chip is wire-bonded with a GaAs PV cell, which generates 893 nA at 1.67 V when exposed to 850 nm light of intensity 120.5 μW/mm². Its data uplink is facilitated by an on-probe LED, whose light is received by a single-photon avalanche diode (SPAD) of the repeater [38]. One of the major advantages of powering through IR is its more uniform coverage in comparison to its EM counterpart. When multiple coils are placed to cover a large area, the EM wave is not uniform and null lines will appear near the borders of the coils. Another difference resulted from the choice of powering schemes is that, for IR, the total received power is proportional to the volume of the PV cells while for EM, the area of the chip is the dominating factor. Instead of measuring all trajectories of the neural action potentials, the system detects spike by using its new spike detector, which is one of the most power efficient and effective developed to date and achieved extremely low backward data rate. Through the use

of both IR powering and spike detection, the total size can be significantly reduced.

Several millimeter-scale BCI systems targeted for neural stimulation have also been developed. The combined electrical/optical stimulator of 39-mm^2 size and 78-mg weight provides a multi-modality stimulation platform that is equipped with both cell-type specific stimulation (optical) and stimulation of larger numbers of nerve fibers (electrical) [203]. The implanted device is powered through ultrasound, and includes a piezoelectric receiver, ASIC, off-chip capacitor, two platinum stimulating electrodes, and an LED. The current-controlled stimulation is externally programmable, amplitude of stimulating current, pulse-width, repetition rate, and optical intensity being able to be adjusted. The maximum achievable electrical stimulation current is 5 mA, and that of optical stimulation intensity is 23 mW/mm^2 [203]. However, due to the focused nature of the transmitter, the implant is subjected to misalignment, which could be improved by incorporating ultrasound imaging and transmit beamforming to the external device to better direct the ultrasound beam to the target. The acceptance angle of the piezoelectric crystals also has to be increased and the ultrasound transfer array optimized to enhance the robustness of the link.

Another example system is the Free-Floating, Wirelessly powered, Implantable Optical Stimulation (FF-WIOS) device with a volume of 9.4 mm^3 and a weight of 15 mg, which has been developed for optogenetic stimulation. The device is powered inductively through a 3-coil link at 60 MHz, with a high Q-factor resonator serving as the relay station. Each FF-WIOS is equipped with 16 stimulation channels (4×4 μLEDs array) and is composed of a System-on-Chip (SoC), off-chip capacitors (utilized to satisfy the high instantaneous power requirement for LEDs), receiver coil, and μLEDs, which are all hermetically-sealed with Parylene-C and polydimethylsiloxane (PDMS). The optical stimulation patterns, including current level, frequency, pulse width, selectively turn on/off specific LEDs, can be configured through on-off-keying at 50 kbps data rate. The power control loop is then closed through sending the rectified signal back to the external headstage at 160 bps data rate via load-shift-keying. Light intensity of up to 10 mW/mm^2 can be achieved. Though *in vivo* experiments were conducted on the larger version of FF-WIOS ($8 \times 14 \times 2$ mm^3) to evaluate its efficacy, the miniaturized version was only tested *in vitro*. Future work focuses on further reducing the power consumption of FF-WIOS through ultra-low power circuit designs [204].

Although most state-of-the-art neural interfaces were developed to have one single function, either neural recording or stimulating, devices that combine both functionality have been designed. Encapsulated neural interfacing acquisition chip (ENIAC) of 3×3-mm^2 size integrates all components into a single chip, including electrodes, antenna, and other circuit components, so that no external off-chip element is required. The 2-coil link is operated using electromagnetic near-field at 144 MHz and is shared for both power

transmission and bidirectional data communication. An integrated resonant regulating rectifier IR^3 is implemented to increase energy efficiency [63], [207]. Each of 16 electrodes, which are directly integrated on the chip, can be configured to be either a recording or stimulating channel. With the use of platinum model electrodes in differential adiabatic triphasic stimulation, 145 μA of current can be delivered to each electrode channel [33]. However, integrating CMOS coil with active circuits on the ASIC can result in considerable loss due to the creation of extra eddy current loops, which should be avoided with careful design of the metal routing layout [53]. The hermetic encapsulation around the coil also reduces its Q-factor and the PTE of the inductive link, especially at higher frequencies [62]. In addition, the ideal resonant frequency is lowered due to higher parasitic capacitance of the surrounding packages, which can be ameliorated by the automatic resonance tuning (ART) operation to maintain the resonant condition [208].

Microbead of $0.34 \times 0.33 \times 0.08$-mm^3 dimension is one of the smallest neural stimulating implants. Akin to ENIAC, it also utilizes a two-coil inductive link, and integrates all components on a single silicon chip, including electrodes, coil and all the required circuitry. Each Microbead has four electrodes, two for recording and two for stimulation. The electrodes are made of PEDOT:PSS/CNT and the implant is encapsulated with SiO$_2$. With the use of monophasic voltage-mode stimulation, maximum stimulation current of 46 μA can be achieved, and the amount of injected charge can be controlled through altering the pulse width. As Microbead is miniaturized with a volume of only 0.009 mm^3, it can be inserted into the area of interests through a syringe with a 22G needle, which could greatly streamline the insertion process with minimal invasiveness. Its functionality has been tested *in vivo* to stimulate the sciatic nerve of a rat. Although the miniaturization of the implant limits its implantation depth (5.5 mm *in vivo*), the depth-to-volume ratio remains one of the highest in literature. However, the achievable Tx-Rx distances of less than 1 cm might be further reduced when Microbead is implanted in the brain. Another challenge is the lowered overall system efficiency due to leaked current caused by the native oxide that is not thick enough, which needs to be solved by employing the silicon-on-insulator (SOI) process. Hermetic biocompatible coating for the Microbead also remains to be designed and developed to make it more durable in harsh tissue environment [37].

VII. CONCLUSIONS

The development of implantable neural interfaces has brought about new opportunities to investigate the functions of the nervous system both in research and clinical applications. It has also transformed the way we approach neurological or psychological disorders, raising hope for those suffering from such diseases that were once considered untreatable. Free-floating neural implants of miniature size have significantly higher scalability, and can be more

extensively distributed around the targeted region of interest. They are more clinically viable as they cause less disturbance to the body and induce less tissue immune response. In this paper, we highlighted the significance and promising applications of miniaturized neural implants. We called attention to the challenges related to scaling-down of neural implants to the millimeter size in aspects including powering, communication, neural recording, and stimulation. Additionally, we looked into current state-of-the-art millimeter-scale implantable neural interfacing systems at the forefront of research, comparing their respective major specifications, performances, and functionalities. Currently, mm-scale neural implants that are clinically viable and suitable for long-term usage are still lacking. Most state-of-the-art systems are still in stages from conceptualization, proof-of-concept to conducting *in vivo* experiments in rats. Future works in this field focus on addressing the challenges mentioned in this paper to achieve long-term implantation and clinical viability. Packaging, long-term stability, and bio-compatibility of the implants are also critical issues that remain to be overcome and resolved. Robust and reliable miniaturized neural implantable systems will transform how we approach and address challenges associated with the nervous system, opening a new chapter for exciting clinical and research applications.

REFERENCES

[1] M. Olchik, M. Ghisi, A. Ayres, A. Schuh, P. Oppitz, and C. Rieder, "The impact of deep brain stimulation on the quality of life and swallowing in individuals with Parkinson's disease," *Int. Arch. Otorhinolaryngol.*, vol. 22, no. 2, pp. 125–129, Apr. 2018.

[2] B. Kundu, L. Schrock, T. Davis, and P. A. House, "Thalamic deep brain stimulation for essential tremor also reduces voice tremor," *Neuromodulation Technol. Neural Interface*, vol. 21, no. 8, pp. 748–754, Dec. 2018.

[3] L. Sperry, Z. Lin, and K. Shahlaie, "Deep brain stimulation in the management of dystonia: Beyond the world of neurotoxins," *J. Nurse Life Care Planning*, vol. 17, no. 4, pp. 15–20, 2017.

[4] M. Naesström, P. Blomstedt, and O. Bodlund, "A systematic review of psychiatric indications for deep brain stimulation, with focus on major depressive and obsessive-compulsive disorder," *Nordic J. Psychiatry*, vol. 70, no. 7, pp. 483–491, Oct. 2016.

[5] M. Sprengers, K. Vonck, E. Carrette, A. G. Marson, and P. Boon, "Deep brain and cortical stimulation for epilepsy," *Cochrane Database Systematic Rev.*, vol. 7, no. 6, Jul. 2017, Art. no. CD008497.

[6] M. Loreiro, S. Brítez, S. Casco, J. C. Moreno, J. L. Pons, and F. Brunetti, "Neuroprosthetic device for functional training, compensation or rehabilitation of lower limbs during gait," in *Proc. 9th Int. IEEE/EMBS Conf. Neural Eng.*, Mar. 2019, pp. 1183–1186.

[7] M. B. Lee, D. R. Kramer, T. Peng, M. F. Barbaro, C. Y. Liu, S. Kellis, and B. Lee, "Clinical neuroprosthetics: Today and tomorrow," *J. Clin. Neurosci.*, vol. 68, pp. 13–19, Oct. 2019.

[8] E. Leuthardt, J. Ojemann, G. Schalk, and D. Moran, "The emerging world of motor neuroprosthetics: A neurosurgical perspective," *Neurosurgery*, vol. 59, no. 1, pp. 1–13, 2006.

[9] M. C. Mott, J. A. Gordon, and W. J. Koroshetz, "The NIH BRAIN initiative: Advancing neurotechnologies, integrating disciplines," *PLOS Biol.*, vol. 16, no. 11, Nov. 2018, Art. no. e3000066.

[10] M. E. J. Obien, K. Deligkaris, T. Bullmann, D. J. Bakkum, and U. Frey, "Revealing neuronal function through microelectrode array recordings," *Frontiers Neurosci.*, vol. 8, p. 423, Jan. 2015.

[11] A. C. Hoogerwerf and K. D. Wise, "A three-dimensional microelectrode array for chronic neural recording," *IEEE Trans. Biomed. Eng.*, vol. 41, no. 12, pp. 1136–1146, 1994.

[12] M. Leber, J. Körner, C. F. Reiche, M. Yin, R. Bhandari, R. Franklin, S. Negi, and F. Solzbacher, "Advances in penetrating multichannel microelectrodes based on the Utah array platform," in *Neural Interface: Frontiers and Applications* (Advances in Experimental Medicine and Biology), vol. 1101, X. Zheng, Ed. Singapore: Springer, 2019, pp. 1–40.

[13] G. N. Angotzi, F. Boi, A. Lecomte, E. Miele, M. Malerba, S. Zucca, A. Casile, and L. Berdondini, "SiNAPS: An implantable active pixel sensor CMOS-probe for simultaneous large-scale neural recordings," *Biosensors Bioelectron.*, vol. 126, pp. 355–364, Feb. 2019.

[14] C. M. Lopez, "Unraveling the brain with high-density CMOS neural probes: Tackling the challenges of neural interfacing," *IEEE Solid State-Circuits Mag.*, vol. 11, no. 4, pp. 43–50, 2019.

[15] R. Fiáth, B. C. Raducanu, S. Musa, A. Andrei, C. M. Lopez, C. van Hoof, P. Ruther, A. Aarts, D. Horváth, and I. Ulbert, "A silicon-based neural probe with densely-packed low-impedance titanium nitride microelectrodes for ultrahigh-resolution *in vivo* recordings," *Biosensors Bioelectron.*, vol. 106, pp. 86–92, May 2018.

[16] J. Putzeys, S. Musa, C. M. Lopez, B. C. Raducanu, A. Carton, J. De Ceulaer, B. Karsh, J. H. Siegle, N. Van Helleputte, T. D. Harris, and B. Dutta, "Neuropixels data-acquisition system: A scalable platform for parallel recording of 10 000+ electrophysiological signals," *IEEE Trans. Biomed. Circuits Syst.*, vol. 13, no. 6, pp. 1635–1644, Dec. 2019.

[17] B. Dutta, A. Andrei, T. D. Harris, C. M. Lopez, J. O'Callahan, J. Putzeys, B. C. Raducanu, S. Severi, S. D. Stavisky, E. M. Trautmann, M. Welkenhuysen, and K. V. Shenoy, "The neuropixels probe: A CMOS based integrated microsystems platform for neuroscience and brain-computer interfaces," in *IEDM Tech. Dig.*, Dec. 2019, pp. 10.1.1–10.1.4.

[18] A. Khalifa, Y. Karimi, Q. Wang, S. Garikapati, W. Montlouis, M. Stanacevic, N. Thakor, and R. Etienne-Cummings, "The microbead: A highly miniaturized wirelessly powered implantable neural stimulating system," *IEEE Trans. Biomed. Circuits Syst.*, vol. 12, no. 3, pp. 521–531, Jun. 2018.

[19] W. W. Seeley, R. K. Crawford, J. Zhou, B. L. Miller, and M. D. Greicius, "Neurodegenerative diseases target large-scale human brain networks," *Neuron*, vol. 62, no. 1, pp. 42–52, Apr. 2009.

[20] L. R. Hochberg, M. D. Serruya, G. M. Friehs, J. A. Mukand, M. Saleh, A. H. Caplan, A. Branner, D. Chen, R. D. Penn, and J. P. Donoghue, "Neuronal ensemble control of prosthetic devices by a human with tetraplegia," *Nature*, vol. 442, no. 7099, pp. 164–171, Jul. 2006.

[21] J. Thelin, H. Jörntell, E. Psouni, M. Garwicz, J. Schouenborg, N. Danielsen, and C. E. Linsmeier, "Implant size and fixation mode strongly influence tissue reactions in the CNS," *PLoS ONE*, vol. 6, no. 1, pp. 1–10, Jan. 2011.

[22] D. Seo, J. M. Carmena, J. M. Rabaey, M. M. Maharbiz, and E. Alon, "Model validation of untethered, ultrasonic neural dust motes for cortical recording," *J. Neurosci. Methods*, vol. 244, pp. 114–122, Apr. 2015.

[23] T. D. Y. Kozai, A. S. Jaquins-Gerstl, A. L. Vazquez, A. C. Michael, and X. T. Cui, "Brain tissue responses to neural implants impact signal sensitivity and intervention strategies," *ACS Chem. Neurosci.*, vol. 6, no. 1, pp. 48–67, Jan. 2015.

[24] K. Famm, B. Litt, K. J. Tracey, E. S. Boyden, and M. Slaoui, "A jump-start for electroceuticals," *Nature*, vol. 496, no. 7444, pp. 159–161, Apr. 2013.

[25] S. Groiss, L. Wojtecki, M. Südmeyer, and A. Schnitzler, "Review: Deep brain stimulation in Parkinson's disease," *Therapeutic Adv. Neurological Disorders*, vol. 2, no. 6, pp. 379–391, 2009.

[26] E. Ben-Menachem, "Vagus nerve stimulation, side effects, and long-term safety," *J. Clin. Neurophysiol.*, no. 5, p. 415, 2001.

[27] M. Ghovanloo and K. Najafi, "A wireless implantable multichannel microstimulating system-on-a-chip with modular architecture," *IEEE Trans. Neural Syst. Rehabil. Eng.*, vol. 15, no. 3, pp. 449–457, Sep. 2007.

[28] S. Kim, R. Bhandari, M. Klein, S. Negi, L. Rieth, P. Tathireddy, M. Toepper, H. Oppermann, and F. Solzbacher, "Integrated wireless neural interface based on the Utah electrode array," *Biomed. Microdevices*, vol. 11, no. 2, pp. 66–453, Apr. 2009. [Online]. Available: http://www.ncbi.nlm.nih.gov/pubmed/19067174

[29] R. M. Walker, H. Gao, P. Nuyujukian, K. Makinwa, K. V. Shenoy, T. Meng, and B. Murmann, "A 96-channel full data rate direct neural interface in 0.13 μm cmos," in *Symp. VLSI Circuits-Dig. Tech. Papers*, 2011, pp. 144–145.

[30] C. M. Lopez, D. Prodanov, D. Braeken, I. Gligorijevic, W. Eberle, C. Bartic, R. Puers, and G. Gielen, "A multichannel integrated circuit for electrical recording of neural activity, with independent channel programmability," *IEEE Trans. Biomed. Circuits Syst.*, vol. 6, no. 2, pp. 101–110, Apr. 2012.

[31] W.-M. Chen, H. Chiueh, T.-J. Chen, C.-L. Ho, C. Jeng, M.-D. Ker, C.-Y. Lin, Y.-C. Huang, C.-W. Chou, T.-Y. Fan, M.-S. Cheng, Y.-L. Hsin, S.-F. Liang, Y.-L. Wang, F.-Z. Shaw, Y.-H. Huang, C.-H. Yang, and C.-Y. Wu, "A fully integrated 8-channel closed-loop neural-prosthetic CMOS SoC for real-time epileptic seizure control," *IEEE J. Solid-State Circuits*, vol. 49, no. 1, pp. 232–247, Jan. 2014.

[32] C. M. Lopez, A. Andrei, S. Mitra, M. Welkenhuysen, W. Eberle, C. Bartic, R. Puers, R. F. Yazicioglu, and G. G. E. Gielen, "An implantable 455-active-electrode 52-channel CMOS neural probe," *IEEE J. Solid-State Circuits*, vol. 49, no. 1, pp. 248–261, Jan. 2014.

[33] S. Ha, A. Akinin, J. Park, C. Kim, H. Wang, C. Maier, P. P. Mercier, and G. Cauwenberghs, "Silicon-integrated high-density electrocortical interfaces," *Proc. IEEE*, vol. 105, no. 1, pp. 11–33, Jan. 2017.

[34] D. Seo, R. M. Neely, K. Shen, U. Singhal, E. Alon, J. M. Rabaey, J. M. Carmena, and M. M. Maharbiz, "Wireless recording in the peripheral nervous system with ultrasonic neural dust," *Neuron*, vol. 91, no. 3, pp. 529–539, Aug. 2016.

[35] T. Tokuda, T. Ishizu, W. Nattakarn, M. Haruta, T. Noda, K. Sasagawa, M. Sawan, and J. Ohta, "1 mm3-sized optical neural stimulator based on CMOS integrated photovoltaic power receiver," *AIP Adv.*, vol. 8, no. 4, Apr. 2018, Art. no. 045018.

[36] V. W. Leung, L. Cui, S. Alluri, J. Lee, J. Huang, E. Mok, S. Shellhammer, R. Rao, P. Asbeck, P. P. Mercier, L. Larson, A. Nurmikko, and F. Laiwalla, "Distributed microscale brain implants with wireless power transfer and mbps bi-directional networked communications," in *Proc. IEEE Custom Integr. Circuits Conf.*, Apr. 2019, pp. 1–4.

[37] A. Khalifa, Y. Liu, Y. Karimi, Q. Wang, A. Eisape, M. Stanaćević, N. Thakor, Z. Bao, and R. Etienne-Cummings, "The microbead: A 0.009 mm^3 implantable wireless neural stimulator," *IEEE Trans. Biomed. Circuits Syst.*, vol. 13, no. 5, pp. 971–985, Oct. 2019.

[38] J. Lim, E. Moon, M. Barrow, S. R. Nason, P. R. Patel, P. G. Patil, S. Oh, I. Lee, H.-S. Kim, D. Sylvester, D. Blaauw, C. A. Chestek, J. Phillips, and T. Jang, "A 0.19×0.17 mm^2 wireless neural recording IC for motor prediction with near-infrared-based power and data telemetry," in *IEEE Int. Solid-State Circuits Conf. (ISSCC) Dig. Tech. Papers*, Feb. 2020, pp. 416–418.

[39] Y. Fang, W. Hou, W. Zhou, and H. Zhang, "Advances in implantable medical device battery," *Chin. J. Med. Instrum.*, vol. 42, no. 4, pp. 272–275, 2018.

[40] C. van Riesen, G. Tsironis, D. Gruber, F. Klostermann, P. Krause, G. H. Schneider, and A. Kupsch, "Disease-specific longevity of impulse generators in deep brain stimulation and review of the literature," *J. Neural Transmiss.*, vol. 123, no. 6, pp. 621–630, Jun. 2016.

[41] S. D. Israeli-Korn, T. Fay-Karmon, S. Tessler, G. Yahalom, S. Benizri, H. Strauss, Z. Zibly, R. Spiegelmann, and S. Hassin-Baer, "Decreasing battery life in subthalamic deep brain stimulation for Parkinson's disease with repeated replacements: Just a matter of energy delivered?" *Brain Stimulation*, vol. 12, no. 4, pp. 845–850, 2019.

[42] M. Niemann, G.-H. Schneider, A. Kühn, P. Vajkoczy, and K. Faust, "Longevity of implantable pulse generators in bilateral deep brain stimulation for movement disorders," *Neuromodulation Technol. Neural Interface*, vol. 21, no. 6, pp. 597–603, Aug. 2018.

[43] K. Bhargava, V. Arora, A. Jaswal, and A. Vora, "Premature battery depletion with St. Jude medical ICD and CRT-D devices: Indian heart rhythm society guidelines for physicians," *Indian Heart J.*, vol. 71, no. 1, pp. 12–14, Jan. 2019.

[44] C. Algora and R. Peña, "Recharging the battery of implantable biomedical devices by light," *Artif. Organs*, vol. 33, no. 10, pp. 855–860, Oct. 2009.

[45] A. Denisov and E. Yeatman, "Ultrasonic vs. inductive power delivery for miniature biomedical implants," in *Proc. Int. Conf. Body Sensor Netw.*, Jun. 2010, pp. 84–89.

[46] D. C. Bock, A. C. Marschilok, K. J. Takeuchi, and E. S. Takeuchi, "Batteries used to power implantable biomedical devices," *Electrochim. Acta*, vol. 84, pp. 155–164, Dec. 2012.

[47] *Donna Marquard, Public Relations or Jon Pike, Public Relations or Jeff Warren, Investor Relations, Medtronic Announces Launch of Activa SC Deep Brain Stimulation System*, Business Wire, Medtronic, Inc., Dublin, Ireland, 2011.

[48] O. Waln and J. Jimenez-Shahed, "Rechargeable deep brain stimulation implantable pulse generators in movement disorders: Patient satisfaction and conversion parameters," *Neuromodulation*, vol. 17, no. 5, pp. 425–430, 2014.

[49] F. Jia, H. Hao, F. Meng, Y. Guo, S. Zhang, J. Zhang, and L. Li, "Patient perspectives on the efficacy of a new kind of rechargeable deep brain stimulators," *Int. J. Neurosci.*, vol. 126, no. 11, pp. 996–1001, 2016.

[50] T. Khaleeq, H. Hasegawa, M. Samuel, and K. Ashkan, "Fixed–life or rechargeable battery for deep brain stimulation: Which do patients prefer?" *Neuromodulation Technol. Neural Interface*, vol. 22, no. 4, pp. 489–492, Jun. 2019.

[51] Boston Scientific. *Precision Spectra Spinal Cord Stimulation System: Information for Prescribers*. Accessed: Oct. 20, 2019. [Online]. Available: https://www.bostonscientific.com

[52] H. Kim, H. Hirayama, S. Kim, K. J. Han, R. Zhang, and J. Choi, "Review of near-field wireless power and communication for biomedical applications," *IEEE Access*, vol. 5, pp. 21264–21285, 2017.

[53] J. Park, C. Kim, A. Akinin, S. Ha, G. Cauwenberghs, and P. P. Mercier, "Wireless powering of mm-scale fully-on-chip neural interfaces," in *Proc. IEEE Biomed. Circuits Syst. Conf.*, Mar. 2017, pp. 1–4.

[54] T. Gerrits, D. C. J. Krop, L. Encica, and E. A. Lomonova, "Development of a linear position independent inductive energy transfer system," in *Proc. IEEE Int. Electric Mach. Drives Conf. (IEMDC)*, May 2011, pp. 1445–1449.

[55] S.-H. Lee and R. D. Lorenz, "Development and validation of model for 95%-efficiency 220-W wireless power transfer over a 30-cm air gap," *IEEE Trans. Ind. Appl.*, vol. 47, no. 6, pp. 2495–2504, Dec. 2011.

[56] H. Kassiri, S. Tonekaboni, M. T. Salam, N. Soltani, K. Abdelhalim, J. L. P. Velazquez, and R. Genov, "Closed-loop neurostimulators: A survey and a seizure-predicting design example for intractable epilepsy treatment," *IEEE Trans. Biomed. Circuits Syst.*, vol. 11, no. 5, pp. 1026–1040, Oct. 2017.

[57] T. Hamed and M. Maqsood, "SAR calculation & temperature response of human body exposure to electromagnetic radiations at 28, 40 and 60 GHz mmWave frequencies," *Prog. Electromagn. Res. M*, vol. 73, pp. 47–59, Jul. 2018.

[58] O. P. Gandhi, "Electromagnetic fields: Human safety issues," *Annu. Rev. Biomed. Eng.*, vol. 4, no. 1, pp. 211–234, Aug. 2002.

[59] G. Lazzi, "Thermal effects of bioimplants," *IEEE Eng. Med. Biol. Mag.*, vol. 24, no. 5, pp. 75–81, Sep. 2005.

[60] R.-F. Xue, K.-W. Cheng, and M. Je, "High-efficiency wireless power transfer for biomedical implants by optimal resonant load transformation," *IEEE Trans. Circuits Syst. I, Reg. Papers*, vol. 60, no. 4, pp. 867–874, Apr. 2013.

[61] D. Laqua, T. Just, and P. Husar, "Measuring the attenuation characteristics of biological tissues enabling for low power *in vivo* RF transmission," in *Proc. Annu. Int. Conf. IEEE Eng. Med. Biol.*, Aug. 2010, pp. 1437–1440.

[62] P. Feng, P. Yeon, Y. Cheng, M. Ghovanloo, and T. G. Constandinou, "Chip-scale coils for millimeter-sized bio-implants," *IEEE Trans. Biomed. Circuits Syst.*, vol. 12, no. 5, pp. 1088–1099, Oct. 2018.

[63] C. Kim, S. Ha, J. Park, A. Akinin, P. P. Mercier, and G. Cauwenberghs, "A 144-MHz fully integrated resonant regulating rectifier with hybrid pulse modulation for mm-sized implants," *IEEE J. Solid-State Circuits*, vol. 52, no. 11, pp. 3043–3055, Nov. 2017.

[64] N. K. Mandloi and S. Ha, "Magnetically balanced power and data telemetry for mm-scale neural implants," in *Proc. 40th Annu. Int. Conf. IEEE Eng. Med. Biol. Soc.*, Jul. 2018, pp. 3378–3381.

[65] P. Yeon, S. Mirbozorgi, B. Ash, H. Eckhardt, and M. Ghovanloo, "Fabrication and microassembly of a mm-sized floating probe for a distributed wireless neural interface," *Micromachines*, vol. 7, no. 9, p. 154, Sep. 2016.

[66] M. Kiani, U.-M. Jow, and M. Ghovanloo, "Design and optimization of a 3-coil inductive link for efficient wireless power transmission," *IEEE Trans. Biomed. Circuits Syst.*, vol. 5, no. 6, pp. 579–591, Dec. 2011.

[67] P. Yeon, S. A. Mirbozorgi, and M. Ghovanloo, "Optimal design of a 3-coil inductive link for millimeter-sized biomedical implants," in *Proc. IEEE Biomed. Circuits Syst. Conf.*, Oct. 2016, pp. 396–399.

[68] J. S. Ho and A. S. Y. Poon, "Conformal microwave lens for focusing across inhomogenous tissue," in *Proc. IEEE Int. Symp. Antennas Propag.*, Jun. 2016, pp. 881–882.

[69] X. Qing, C. K. Goh, and Z. N. Chen, "A broadband UHF near-field RFID antenna," *IEEE Trans. Antennas Propag.*, vol. 58, no. 12, pp. 3829–3838, Dec. 2010.

[70] S. A. Mirbozorgi, P. Yeon, and M. Ghovanloo, "Robust wireless power transmission to mm-sized free-floating distributed implants," *IEEE Trans. Biomed. Circuits Syst.*, vol. 11, no. 3, pp. 692–702, Jun. 2017.

[71] R. Sarpeshkar, *Ultra Low Power Bioelectronics: Fundamentals, Biomedical Applications, and Bio-Inspired Systems*. Cambridge, U.K.: Cambridge Univ. Press, 2013.

[72] A. B. Amar, A. B. Kouki, and H. Cao, "Power approaches for implantable medical devices," *Sensors*, vol. 15, no. 11, pp. 28889–28914, 2015.

[73] M. G. L. Roes, J. L. Duarte, M. A. M. Hendrix, and E. A. Lomonova, "Acoustic energy transfer: A review," *IEEE Trans. Ind. Electron.*, vol. 60, no. 1, pp. 242–248, Jan. 2013.

[74] P. J. Larson and B. C. Towe, "Miniature ultrasonically powered wireless nerve cuff stimulator," in *Proc. Int. IEEE/EMBS Conf. Neural Eng.*, Apr. 2011, pp. 265–268.

[75] A. Ibrahim, M. Meng, and M. Kiani, "A comprehensive comparative study on inductive and ultrasonic wireless power transmission to biomedical implants," *IEEE Sensors J.*, vol. 18, no. 9, pp. 3813–3826, May 2018.

[76] V. F.-G. Tseng, S. S. Bedair, and N. Lazarus, "Phased array focusing for acoustic wireless power transfer," *IEEE Trans. Ultrason., Ferroelectr., Freq. Control*, vol. 65, no. 1, pp. 39–49, Jan. 2018.

[77] T. C. Chang, M. J. Weber, J. Charthad, S. Baltsavias, and A. Arbabian, "Scaling of ultrasound-powered receivers for sub-millimeter wireless implants," in *Proc. IEEE Biomed. Circuits Syst. Conf.*, Oct. 2017, pp. 1–4.

[78] T. R. Nelson, J. B. Fowlkes, J. S. Abramowicz, and C. C. Church, "Ultrasound biosafety considerations for the practicing sonographer and sonologist," *J. Ultrasound Med.*, vol. 28, no. 2, pp. 139–150, Feb. 2009. [Online]. Available: https://onlinelibrary.wiley.com/doi/abs/10.7863/jum.2009.28.2.139

[79] C. Pasquinelli, L. G. Hanson, H. R. Siebner, H. J. Lee, and A. Thielscher, "Safety of transcranial focused ultrasound stimulation: A systematic review of the state of knowledge from both human and animal studies," *Brain Stimulation*, vol. 12, no. 6, pp. 1367–1380, Nov. 2019. [Online]. Available: http://www.sciencedirect.com/science/article/pii/S1935861X19303389

[80] G. Pinton, J.-F. Aubry, E. Bossy, M. Muller, M. Pernot, and M. Tanter, "Attenuation, scattering, and absorption of ultrasound in the skull bone," *Med. Phys.*, vol. 39, no. 1, pp. 299–307, Dec. 2011.

[81] B. M. G. Rosa and G.-Z. Yang, "Ultrasound powered implants: Design, performance considerations and simulation results," *Sci. Rep.*, vol. 10, no. 1, pp. 1–16, Dec. 2020.

[82] Q. He, J. Liu, B. Yang, X. Wang, X. Chen, and C. Yang, "MEMS-based ultrasonic transducer as the receiver for wireless power supply of the implantable microdevices," *Sens. Actuators A, Phys.*, vol. 219, pp. 65–72, Nov. 2014. [Online]. Available: http://www.sciencedirect.com/science/article/pii/S0924424714003380

[83] K. Murakawa, M. Kobayashi, O. Nakamura, and S. Kawata, "A wireless near-infrared energy system for medical implants," *IEEE Eng. Med. Biol. Mag.*, vol. 18, no. 6, pp. 70–72, Nov. 1999.

[84] H. Kanai, "Properties of biomaterials (7). Optical properties," *Iyodenshi To Seitai Kogaku, Jpn. J. Med. Electron. Biol. Eng.*, vol. 15, no. 1, pp. 48–56, Feb. 1977

[85] K. Goto, T. Nakagawa, O. Nakamura, and S. Kawata, "An implantable power supply with an optically rechargeable lithium battery," *IEEE Trans. Biomed. Eng.*, vol. 48, no. 7, pp. 830–833, Jul. 2001.

[86] E. Moon, D. Blaauw, and J. D. Phillips, "Subcutaneous photovoltaic infrared energy harvesting for bio-implantable devices," *IEEE Trans. Electron Devices*, vol. 64, no. 5, pp. 2432–2437, May 2017.

[87] S. Ayazian and A. Hassibi, "Delivering optical power to subcutaneous implanted devices," in *Proc. Annu. Int. Conf. IEEE Eng. Med. Biol. Soc.*, Aug. 2011, pp. 2874–2877.

[88] S. L. Jacques, "Optical properties of biological tissues: A review," *Phys. Med. Biol.*, vol. 58, no. 11, pp. R37–R61, May 2013.

[89] E. Moon, D. Blaauw, and J. D. Phillips, "Small-area Si photovoltaics for low-flux infrared energy harvesting," *IEEE Trans. Electron Devices*, vol. 64, no. 1, pp. 15–20, Jan. 2017.

[90] S. Golovynskyi, I. Golovynska, L. I. Stepanova, O. I. Datsenko, L. Liu, J. Qu, and T. Y. Ohulchanskyy, "Optical windows for head tissues in near-infrared and short-wave infrared regions: Approaching transcranial light applications," *J. Biophotonics*, vol. 11, no. 12, Dec. 2018, Art. no. e201800141.

[91] P. Feng and T. G. Constandinou, "Robust wireless power transfer to multiple mm-scale freely-positioned neural implants," in *Proc. IEEE Biomed. Circuits Syst. Conf.*, Oct. 2018, pp. 1–4.

[92] P. Yeon, M. S. Bakir, and M. Ghovanloo, "Towards a 1.1 mm² free-floating wireless implantable neural recording SoC," in *Proc. IEEE Custom Integr. Circuits Conf.*, Apr. 2018, pp. 1–4.

[93] J. Lee, E. Mok, J. Huang, L. Cui, A.-H. Lee, V. Leung, P. Mercier, S. Shellhammer, L. Larson, P. Asbeck, R. Rao, Y.-K. Song, A. Nurmikko, and F. Laiwalla, "An implantable wireless network of distributed microscale sensors for neural applications," in *Proc. 9th Int. IEEE/EMBS Conf. Neural Eng.*, Mar. 2019, pp. 871–874.

[94] N. Ahmadi, M. L. Cavuto, P. Feng, L. B. Leene, M. Maslik, F. Mazza, O. Savolainen, K. M. Szostak, C.-S. Bouganis, J. Ekanayake, A. Jackson, and T. G. Constandinou, "Towards a distributed, chronically-implantable neural interface," in *Proc. 9th Int. IEEE/EMBS Conf. Neural Eng.*, Mar. 2019, pp. 719–724.

[95] J. Lee, J. Jang, and Y.-K. Song, "A review on wireless powering schemes for implantable microsystems in neural engineering applications," *Biomed. Eng. Lett.*, vol. 6, no. 4, pp. 205–215, Nov. 2016.

[96] B. I. Rapoport, J. T. Kedzierski, and R. Sarpeshkar, "A glucose fuel cell for implantable brain-machine interfaces," *PLoS ONE*, vol. 7, no. 6, pp. 1–15, 2012.

[97] S. K. Chaudhuri and D. R. Lovley, "Electricity generation by direct oxidation of glucose in mediatorless microbial fuel cells," *Nature Biotechnol.*, vol. 21, no. 10, p. 1229, 2003.

[98] L. Beker, A. Benet, A. T. Meybodi, B. Eovino, A. P. Pisano, and L. Lin, "Energy harvesting from cerebrospinal fluid pressure fluctuations for self-powered neural implants," *Biomed. Microdevices*, vol. 19, no. 2, p. 32, Apr. 2017, doi: 10.1007/s10544-017-0176-1.

[99] P. P. Mercier, A. C. Lysaght, S. Bandyopadhyay, A. P. Chandrakasan, and K. M. Stankovic, "Energy extraction from the biologic battery in the inner ear," *Nature Biotechnol.*, vol. 30, no. 12, pp. 1240–1243, Dec. 2012.

[100] H. Yu and K. Najafi, "Low-power interface circuits for bio-implantable microsystems," in *Proc. IEEE Int. Solid-State Circuits Conf., . Dig. Tech. Papers. ISSCC.*, Feb. 2003, pp. 194–487.

[101] M. S. E. Sendi, M. Judy, H. Molaei, A. M. Sodagar, and M. Sharifkhani, "Wireless interfacing to cortical neural recording implants using 4-FSK modulation scheme," in *Proc. IEEE Int. Conf. Electron., Circuits, Syst.*, Dec. 2015, pp. 221–224.

[102] D. Kim, M. Ko, D. Ng, and W.-Y. Choi, "A single-bit sampling demodulator for biomedical implants," *Microelectron. J.*, vol. 46, no. 8, pp. 669–673, Aug. 2015.

[103] J. Tan, W.-S. Liew, C.-H. Heng, and Y. Lian, "A 2.4 GHz ULP reconfigurable asymmetric transceiver for single-chip wireless neural recording IC," *IEEE Trans. Biomed. Circuits Syst.*, vol. 8, no. 4, pp. 497–509, Aug. 2014.

[104] S. A. Mirbozorgi, H. Bahrami, M. Sawan, L. A. Rusch, and B. Gosselin, "A single-chip full-duplex high speed transceiver for multi-site stimulating and recording neural implants," *IEEE Trans. Biomed. Circuits Syst.*, vol. 10, no. 3, pp. 643–653, Jun. 2016.

[105] Z. Tang, B. Smith, J. H. Schild, and P. H. Peckham, "Data transmission from an implantable biotelemeter by load-shift keying using circuit configuration modulator," *IEEE Trans. Biomed. Eng.*, vol. 42, no. 5, pp. 524–528, May 1995.

[106] S. Mandal and R. Sarpeshkar, "Power-efficient impedance-modulation wireless data links for biomedical implants," *IEEE Trans. Biomed. Circuits Syst.*, vol. 2, no. 4, pp. 301–315, Dec. 2008.

[107] S. Ha, C. Kim, J. Park, S. Joshi, and G. Cauwenberghs, "Energy-recycling integrated 6.78-Mbps data 6.3-mW power telemetry over a single 13.56-MHz inductive link," in *Symp. VLSI Circuits Dig. Tech. Papers*, Jun. 2014.

[108] J. Zhou and J. Chen, "Maximum distance estimation of far-field model for underwater magnetic field communication," in *Proc. IEEE Annu. Comput. Commun. Workshop Conf.*, Jan. 2017, pp. 1–5.

[109] K. Jin, Z. Geng, J. Zheng, Y. Liu, Z. Yang, and X. He, "Analysis of dualport reader antenna for UHF RFID near-field and far-field applications," *Prog. Electromagn. Res. M*, vol. 72, pp. 31–40, 2018.

[110] J. L. Bohorquez, A. P. Chandrakasan, and J. L. Dawson, "A 350 μw CMOS MSK transmitter and 400 μW OOK super-regenerative receiver for medical implant communications," *IEEE J. Solid-State Circuits*, vol. 44, no. 4, pp. 1248–1259, Apr. 2009.

[111] F. Chen, A. P. Chandrakasan, and V. M. Stojanovic, "Design and analysis of a hardware-efficient compressed sensing architecture for data compression in wireless sensors," *IEEE J. Solid-State Circuits*, vol. 47, no. 3, pp. 744–756, Mar. 2012.

[112] F. Goodarzy, E. Skafidas, and S. Gambini, "Feasibility of energy-autonomous wireless microsensors for biomedical applications: Powering and communication," *IEEE Rev. Biomed. Eng.*, vol. 8, pp. 17–29, 2015.

[113] J. R. Fernandes and D. Wentzloff, "Recent advances in IR-UWB transceivers: An overview," in *Proc. IEEE Int. Symp. Circuits Syst.*, May 2010, pp. 3284–3287.

[114] Y. Gao, Y. Zheng, S. Diao, W.-D. Toh, C.-W. Ang, M. Je, and C.-H. Heng, "Low-power ultrawideband wireless telemetry transceiver for medical sensor applications," *IEEE Trans. Biomed. Eng.*, vol. 58, no. 3, pp. 768–772, Mar. 2011.

[115] *Revision of Part 15 of the Commissions Rules Regarding Ultra-Wideband Transmission Systems*, First Report and Order, ET Docket, US Federal Communications Commission, 2002, pp. 98–153.

[116] A. P. Chandrakasan, F. S. Lee, D. D. Wentzloff, V. Sze, B. P. Ginsburg, P. P. Mercier, D. C. Daly, and R. Blazquez, "Low-power impulse UWB architectures and circuits," *Proc. IEEE*, vol. 97, no. 2, pp. 332–352, Feb. 2009.

[117] H. Ando, K. Takizawa, T. Yoshida, K. Matsushita, M. Hirata, and T. Suzuki, "Multichannel neural recording with a 128 mbps UWB wireless transmitter for implantable brain-machine interfaces," in *Proc. 37th Annu. Int. Conf. IEEE Eng. Med. Biol. Soc. (EMBC)*, Aug. 2015, pp. 4097–4100.

[118] Y.-C. Kuan, Y.-K. Lo, Y. Kim, M.-C. Frank Chang, and W. Liu, "Wireless gigabit data telemetry for large-scale neural recording," *IEEE J. Biomed. Health Informat.*, vol. 19, no. 3, pp. 949–957, May 2015.

[119] M. Crepaldi, G. N. Angotzi, A. Maviglia, F. Diotalevi, and L. Berdondini, "A 5 pJ/pulse at 1-Gpps pulsed transmitter based on asynchronous logic Master–Slave PLL synthesis," *IEEE Trans. Circuits Syst. I, Reg. Papers*, vol. 65, no. 3, pp. 1096–1109, Mar. 2018.

[120] M. Crepaldi, G. N. Angotzi, and L. Berdondini, "A 0.34 mm2 1 Gb/s non-coherent UWB receiver architecture with pulse enhancement and double PLL clock/data packet recovery," *IEEE Trans. Circuits Syst. I, Reg. Papers*, vol. 66, no. 7, pp. 2735–2748, Jul. 2019.

[121] N. Chahat, M. Zhadobov, R. Sauleau, and K. Ito, "A compact UWB antenna for on-body applications," *IEEE Trans. Antennas Propag.*, vol. 59, no. 4, pp. 1123–1131, Apr. 2011.

[122] H. Ando, K. Takizawa, T. Yoshida, K. Matsushita, M. Hirata, and T. Suzuki, "Wireless multichannel neural recording with a 128-mbps UWB transmitter for an implantable brain-machine interfaces," *IEEE Trans. Biomed. Circuits Syst.*, vol. 10, no. 6, pp. 1068–1078, Dec. 2016.

[123] Digi-Key Electronics. *Chip Monolithic Ceramic Capacitor for General: GRM033R60J105MEA2*. Accessed: Sep. 15, 2019. [Online]. Available: https://www.digikey.com/product-detail/en/murata-electronics/GRM033R60J105MEA2D/490-7229-1-ND/4213268

[124] S. Ha, C. Kim, J. Park, S. Joshi, and G. Cauwenberghs, "Energy recycling telemetry IC with simultaneous 11.5 mW power and 6.78 Mb/s backward data delivery over a single 13.56 MHz inductive link," *IEEE J. Solid-State Circuits*, vol. 51, no. 11, pp. 2664–2678, Nov. 2016.

[125] M. Dipalo, H. Amin, L. Lovato, F. Moia, V. Caprettini, G. C. Messina, F. Tantussi, L. Berdondini, and F. De Angelis, "Intracellular and extracellular recording of spontaneous action potentials in mammalian neurons and cardiac cells with 3D plasmonic nanoelectrodes," *Nano Lett.*, vol. 17, no. 6, pp. 3932–3939, Jun. 2017.

[126] G. Benoit, "Recent advances in neural recording microsystems," *Sensors*, vol. 11, no. 5, pp. 4572–4597, 2011.

[127] J. T. Robinson, M. Jorgolli, and H. Park, "Nanowire electrodes for high-density stimulation and measurement of neural circuits," *Frontiers Neural Circuits*, vol. 7, p. 38, 2013.

[128] L. López-Jury, R. C. Meza, M. T. C. Brown, P. Henny, and C. C. Canavier, "Morphological and biophysical determinants of the intracellular and extracellular waveforms in nigral dopaminergic neurons: A computational study," *J. Neurosci.*, vol. 38, no. 38, pp. 8295–8310, Sep. 2018.

[129] K. H. Pettersen and G. T. Einevoll, "Amplitude variability and extracellular low-pass filtering of neuronal spikes," *Biophys. J.*, vol. 94, no. 3, pp. 784–802, Feb. 2008.

[130] A. Belitski, A. Gretton, C. Magri, Y. Murayama, M. A. Montemurro, N. K. Logothetis, and S. Panzeri, "Low-frequency local field potentials and spikes in primary visual cortex convey independent visual information," *J. Neurosci.*, vol. 28, no. 22, pp. 5696–5709, May 2008.

[131] A. H. Marblestone, B. M. Zamft, Y. G. Maguire, M. G. Shapiro, T. R. Cybulski, J. I. Glaser, D. Amodei, P. B. Stranges, R. Kalhor, D. A. Dalrymple, D. Seo, E. Alon, M. M. Maharbiz, J. M. Carmena, J. M. Rabaey, E. S. Boyden, G. M. Church, and K. P. Kording, "Physical principles for scalable neural recording," *Frontiers Comput. Neurosci.*, vol. 7, p. 137, Oct. 2013.

[132] T. M. Hall, K. Nazarpour, and A. Jackson, "Real-time estimation and biofeedback of single-neuron firing rates using local field potentials," *Nature Commun.*, vol. 5, no. 1, p. 5462, Dec. 2014.

[133] R. Muller, H. P. Le, W. Li, P. Ledochowitsch, S. Gambini, T. Bjorninen, A. Koralek, J. M. Carmena, M. M. Maharbiz, E. Alon, and J. M. Rabaey, "A minimally invasive 64-channel wireless μ ECoG implant," *IEEE J. Solid-State Circuits*, vol. 50, no. 1, pp. 344–359, Jan. 2015.

[134] M. Gabriel, C. Julien, P. A. Salin, and C. Jean-Christophe, "Differential recordings of local field potential: A genuine tool to quantify functional connectivity," *PLoS ONE*, vol. 13, no. 12, pp. 1–18, Dec. 2018.

[135] S. B. Rutkove, *Introduction to Volume Conduction*. Totowa, NJ, USA: Humana Press, 2007, pp. 43–53.

[136] Y. Kajikawa and C. E. Schroeder, "How local is the local field potential?" *Neuron*, vol. 72, no. 5, pp. 847–858, Dec. 2011.

[137] S. Ski, K. Wójcik, Daniel, J. Tereszczuk, D. A. Wiejkowski, E. Kublik, and A. Wróbel, "Inverse current-source density method in 3D: Reconstruction fidelity, boundary effects, and influence of distant sources," *Neuroinformatics*, vol. 5, no. 4, pp. 22–207, Dec. 2007.

[138] D. Seo, J. M. Carmena, J. M. Rabaey, E. Alon, and M. M. Maharbiz, "Neural dust: An ultrasonic, low power solution for chronic brain-machine interfaces," 2013, *arXiv:1307.2196*. [Online]. Available: http://arxiv.org/abs/1307.2196

[139] H. McCann, G. Pisano, and L. Beltrachini, "Variation in reported human head tissue electrical conductivity values," *Brain Topogr.*, vol. 32, pp. 825–858, 2019. [Online]. Available: https://doi.org/10.1007/s10548-019-00710-2

[140] C. Gold, D. A. Henze, and C. Koch, "Using extracellular action potential recordings to constrain compartmental models," *J. Comput. Neurosci.*, vol. 23, no. 1, pp. 39–58, Jun. 2007.

[141] M. S. J. Steyaert and W. M. C. Sansen, "A micropower low-noise monolithic instrumentation amplifier for medical purposes," *IEEE J. Solid-State Circuits*, vol. 22, no. 6, pp. 1163–1168, Dec. 1987.

[142] D. Han, Y. Zheng, R. Rajkumar, G. S. Dawe, and M. Je, "A 0.45 V 100-channel neural-recording IC with sub-μ W/channel consumption in 0.18 μ m CMOS," *IEEE Trans. Biomed. Circuits Syst.*, vol. 7, no. 6, pp. 735–746, Dec. 2013.

[143] X. Zou, L. Liu, J. H. Cheong, L. Yao, P. Li, M.-Y. Cheng, W. L. Goh, R. Rajkumar, G. S. Dawe, K.-W. Cheng, and M. Je, "A 100-channel 1-mW implantable neural recording IC," *IEEE Trans. Circuits Syst. I, Reg. Papers*, vol. 60, no. 10, pp. 2584–2596, Oct. 2013.

[144] Y. Dong, L. Tang, X. Yang, M. Zhao, P. Sun, and X. Wu, "A 1.8 μW 32 nV/$\sqrt{}$Hz current-reuse capacitively-coupled instrumentation amplifier for EEG detection," in *Proc. IEEE Int. Symp. Circuits Syst.*, May 2017, pp. 1–4.

[145] M. Rezaei, E. Maghsoudloo, C. Bories, Y. De Koninck, and B. Gosselin, "A low-power current-reuse analog front-end for high-density neural recording implants," *IEEE Trans. Biomed. Circuits Syst.*, vol. 12, no. 2, pp. 271–280, Apr. 2018.

[146] G. Fröhlig, "Hochohm-elektroden," *Herzschrittmachertherapi+ Elektrophysiologie*, vol. 12, no. 3, pp. 131–140, Sep. 2001.

[147] Y. M. Chi, C. Maier, and G. Cauwenberghs, "Ultra-high input impedance, low noise integrated amplifier for noncontact biopotential sensing," *IEEE J. Emerg. Sel. Topics Circuits Syst.*, vol. 1, no. 4, pp. 526–535, Dec. 2011.

[148] X. Zhou, Q. Li, S. Kilsgaard, F. Moradi, S. L. Kappel, and P. Kidmose, "A wearable ear-EEG recording system based on dry-contact active electrodes," in *IEEE Symp. VLSI Circuits Dig. Tech. Papers*, Jun. 2016, pp. 1–2.

[149] J. Lee, G.-H. Lee, H. Kim, and S. Cho, "An ultra-high input impedance analog front end using self-calibrated positive feedback," *IEEE J. Solid-State Circuits*, vol. 53, no. 8, pp. 2252–2262, Aug. 2018.

[150] J. Lee, H. Kim, and S. Cho, "A 255 nW ultra-high input impedance analog front-end for non-contact ECG monitoring," in *Proc. IEEE Custom Integr. Circuits Conf. (CICC)*, Apr. 2017, pp. 1–4.

[151] V. Viswam, M. E. J. Obien, F. Franke, U. Frey, and A. Hierlemann, "Optimal electrode size for multi-scale extracellular-potential recording from neuronal assemblies," *Frontiers Neurosci.*, vol. 13, p. 385, Apr. 2019.

[152] M. Hill, E. Rios, S. K. Sudhakar, D. H. Roossien, C. Caldwell, D. Cai, O. J. Ahmed, S. F. Lempka, and C. A. Chestek, "Quantitative simulation of extracellular single unit recording from the surface of cortex," *J. Neural Eng.*, vol. 15, no. 5, Jul. 2018, Art. no. 056007.

[153] S. Mondal and D. A. Hall, "An ECG chopper amplifier achieving 0.92 NEF and 0.85 PEF with AC-coupled inverter-stacking for noise efficiency enhancement," in *Proc. IEEE Int. Symp. Circuits Syst.*, May 2017, pp. 1–4.

[154] D. Budai, "Ultralow-noise headstage and main amplifiers for extracellular spike recording," *Acta Biologica Szegediensis*, vol. 48, nos. 1–4, pp. 13–17, 2004.

[155] P. F. White, S. Li, and J. W. Chiu, "Electroanalgesia: Its role in acute and chronic pain management," *Anesthesia Analgesia Cleveland*, vol. 92, no. 2, pp. 505–513, 2001.

[156] P. M. Lewis and J. V. Rosenfeld, "Electrical stimulation of the brain and the development of cortical visual prostheses: An historical perspective," *Brain Res.*, vol. 1630, pp. 208–224, Jan. 2016.

[157] Z. Li, D. Guiraud, D. Andreu, A. Gelis, C. Fattal, and M. Hayashibe, "Real-time closed-loop functional electrical stimulation control of muscle activation with evoked electromyography feedback for spinal cord injured patients," *Int. J. Neural Syst.*, vol. 28, no. 6, Aug. 2018, Art. no. 1750063.

[158] W. Junao and A. S. Widge, "Neuromodulation approaches to mood disorders," *Psychiatric Times*, vol. 27, no. 2, pp. 22–24, 2020.

[159] A. Bartoli, Y. El Hassani, B. Jenny, S. Momjian, C. M. Korff, M. Seeck, S. Vulliemoz, and K. Schaller, "What to do in failed hemispherotomy? Our clinical series and review of the literature," *Neurosurg. Rev.*, vol. 41, no. 1, pp. 125–132, Jan. 2018.

[160] M. Tuft and K. O. Nakken, "Post-lobotomy epilepsy illustrated by the story of Ellinor Hamsun, the daughter of the famous Norwegian author Knut Hamsun," *Epilepsy Behav. Case Rep.*, vol. 8, pp. 87–91, Sep. 2017, doi: 10.1016/j.ebcr.2017.08.003.

[161] F. J. Santos, R. M. Costa, and F. Tecuapetla, "Stimulation on demand: Closing the loop on deep brain stimulation," *Neuron*, vol. 72, no. 2, pp. 197–198, Oct. 2011.

[162] B. Rosin, M. Slovik, R. Mitelman, M. Rivlin-Etzion, S. N. Haber, Z. Israel, E. Vaadia, and H. Bergman, "Closed-loop deep brain stimulation is superior in ameliorating parkinsonism," *Neuron*, vol. 72, no. 2, pp. 370–384, Oct. 2011.

[163] G. Fröhlig, "High impedance electrodes," *Herzschrittmachertherapie Elektrophysiologie*, vol. 12, no. 3, pp. 131–140, 2001.

[164] E. Castagnola, A. Ansaldo, E. Maggiolini, T. Ius, M. Skrap, D. Ricci, and L. Fadiga, "Smaller, softer, lower-impedance electrodes for human neuroprosthesis: A pragmatic approach," *Frontiers Neuroeng.*, vol. 7, p. 8, 2014.

[165] W. Franks, I. Schenker, P. Schmutz, and A. Hierlemann, "Impedance characterization and modeling of electrodes for biomedical applications," *IEEE Trans. Biomed. Eng.*, vol. 52, no. 7, pp. 1295–1302, Jul. 2005.

[166] Y. Guo, W. Duan, C. Ma, C. Jiang, Y. Xie, H. Hao, R. Wang, and L. Li, "Biocompatibility and magnetic resonance imaging characteristics of carbon nanotube yarn neural electrodes in a rat model," *Biomed. Eng. OnLine*, vol. 14, no. 1, p. 118, Dec. 2015.

[167] G. A. McCallum, X. Sui, C. Qiu, J. Marmerstein, Y. Zheng, T. E. Eggers, C. Hu, L. Dai, and D. M. Durand, "Chronic interfacing with the autonomic nervous system using carbon nanotube (CNT) yarn electrodes," *Sci. Rep.*, vol. 7, no. 1, pp. 1–14, Dec. 2017.

[168] I. Yoon, K. Hamaguchi, I. V. Borzenets, G. Finkelstein, R. Mooney, and B. R. Donald, "Intracellular neural recording with pure carbon nanotube probes," *PLoS ONE*, vol. 8, no. 6, pp. 1–6, 2013.

[169] J. Y. Su, X. Zhang, M. N. Li, T. Gao, R. Wang, X. Y. Chai, D. G. Zhang, X. H. Zhang, and X. H. Sui, "Insulation of carbon nanotube yarn electrodes for intrafascicular neural stimulation and recording," in *Proc. Int. IEEE/EMBS Conf. Neural Eng.*, Mar. 2019, pp. 815–818.

[170] C. Jiang, L. Li, and H. Hao, "Carbon nanotube yarns for deep brain stimulation electrode," *IEEE Trans. Neural Syst. Rehabil. Eng.*, vol. 19, no. 6, pp. 612–616, Dec. 2011.

[171] L. Santos, J. Neto, A. Crespo, P. Baião, P. Barquinha, L. Pereira, R. Martins, and E. Fortunato, "Electrodeposition of WO$_3$ nanoparticles for sensing applications," in *Electroplating of Nanostructures*. Dec. 2015, pp. 1–22, doi: 10.5772/61216.

[172] G. Fröhlig, A. Bolz, J. Ströbel, M. Rutz, P. Lawall, H. Schwerdt, M. Schaldach, H. Schieffer, "A fractally coated, 1.3 mm^2 high impedance pacing electrode," *Pacing Clin. Electrophysiol.*, vol. 21, no. 6, pp. 1239–1246, 1998.

[173] D. N. Heo, S.-J. Lee, R. Timsina, X. Qiu, N. J. Castro, and L. G. Zhang, "Development of 3D printable conductive hydrogel with crystallized PEDOT:PSS for neural tissue engineering," *Mater. Sci. Eng. C*, vol. 99, pp. 582–590, Jun. 2019.

[174] J. P. Neto, P. Baião, G. Lopes, J. Frazão, J. Nogueira, E. Fortunato, P. Barquinha, and A. R. Kampff, "Does impedance matter when recording spikes with polytrodes?" *Frontiers Neurosci.*, vol. 12, p. 715, Oct. 2018.

[175] H. He, L. Zhang, X. Guan, H. Cheng, X. Liu, S. Yu, J. Wei, and J. Ouyang, "Biocompatible conductive polymers with high conductivity and high stretchability," *ACS Appl. Mater. Interfaces*, vol. 11, no. 29, pp. 26185–26193, 2019.

[176] M. Yang, Y. Zhang, H. Zhang, and Z. Li, "Characterization of PEDOT:PSS as a biocompatible conductive material," in *Proc. IEEE Int. Conf. Nano/Micro Engineered Mol. Syst.*, Apr. 2015, pp. 149–151.

[177] R. M. Miriani, M. R. Abidian, and D. R. Kipke, "Cytotoxic analysis of the conducting polymer PEDOT using myocytes," in *Proc. 30th Annu. Int. Conf. IEEE Eng. Med. Biol. Soc.*, Aug. 2008, pp. 1841–1844.

[178] S. Wagner, S. M. Rampersad, Ü. Aydin, J. Vorwerk, T. F. Oostendorp, T. Neuling, C. S. Herrmann, D. F. Stegeman, and C. H. Wolters, "Investigation of tDCS volume conduction effects in a highly realistic head model," *J. Neural Eng.*, vol. 11, no. 1, Feb. 2014, Art. no. 016002.

[179] P. C. Miranda, A. Mekonnen, R. Salvador, and G. Ruffini, "The electric field in the cortex during transcranial current stimulation," *NeuroImage*, vol. 70, pp. 48–58, Apr. 2013.

[180] T. Radman, R. L. Ramos, J. C. Brumberg, and M. Bikson, "Role of cortical cell type and morphology in subthreshold and suprathreshold uniform electric field stimulation in vitro," *Brain Stimulation*, vol. 2, no. 4, pp. 215–228, 2009.

[181] H. Ye and A. Steiger, "Neuron matters: Electric activation of neuronal tissue is dependent on the interaction between the neuron and the electric field," *J. NeuroEng. Rehabil.*, vol. 12, no. 1, pp. 1–9, Dec. 2015.

[182] J. G. Jefferys, "Nonsynaptic modulation of neuronal activity in the brain: Electric currents and extracellular ions," *Physiological Rev.*, vol. 75, no. 4, pp. 689–723, Oct. 1995.

[183] A. Opitz, A. Falchier, C.-G. Yan, E. M. Yeagle, G. S. Linn, P. Megevand, A. Thielscher, R. Deborah, M. P. Milham, A. D. Mehta, and C. E. Schroeder, "Spatiotemporal structure of intracranial electric fields induced by transcranial electric stimulation in humans and nonhuman primates," *Sci. Rep.*, vol. 6, no. 1, Art. no. 31236, Aug. 2016.

[184] G. Ruffini, R. Salvador, E. Tadayon, R. Sanchez-Todo, A. Pascual-Leone, and E. Santarnecchi, "Realistic modeling of ephaptic fields in the human brain," *bioRxiv*, 2019, doi: 10.1101/688101.

[185] Y. Huang, A. A. Liu, B. Lafon, D. Friedman, M. Dayan, X. Wang, M. Bikson, W. K. Doyle, O. Devinsky, and L. C. Parra, "Measurements and models of electric fields in the *in vivo* human brain during transcranial electric stimulation," *eLife*, vol. 6, p. e18834, Feb. 2017.

[186] M. T. Alt, E. Fiedler, L. Rudmann, J. S. Ordonez, P. Ruther, and T. Stieglitz, "Let there be light—Optoprobes for neural implants," *Proc. IEEE*, vol. 105, no. 1, pp. 101–138, Jan. 2017.

[187] K. Deisseroth, "Optogenetics," *Nature Methods*, vol. 8, no. 1, p. 26, 2011.

[188] R. L. Fork, "Laser stimulation of nerve cells in Aplysia," *Science*, vol. 171, no. 3974, pp. 907–908, Mar. 1971.

[189] O. Yizhar, L. E. Fenno, T. J. Davidson, M. Mogri, and K. Deisseroth, "Optogenetics in neural systems," *Neuron*, vol. 71, no. 1, pp. 9–34, Jul. 2011.

[190] T. Wu, C.-W. Sher, Y. Lin, C.-F. Lee, S. Liang, Y. Lu, S.-W. Huang Chen, W. Guo, H.-C. Kuo, and Z. Chen, "Mini-LED and micro-LED: Promising candidates for the next generation display technology," *Appl. Sci.*, vol. 8, no. 9, p. 1557, Sep. 2018.

[191] J. W. Reddy, I. Kimukin, E. Towe, and M. Chamanzar, "Flexible, monolithic, high-density LED neural probes for simultaneous optogenetics stimulation and recording," in *Proc. 9th Int. IEEE/EMBS Conf. Neural Eng.*, Mar. 2019, pp. 831–834.

[192] F. Wu, E. Stark, P.-C. Ku, K. D. Wise, G. Buzsáki, and E. Yoon, "Monolithically integrated μ LEDs on silicon neural probes for high-resolution optogenetic studies in behaving animals," *Neuron*, vol. 88, no. 6, pp. 1136–1148, Dec. 2015.

[193] K. Kim, D. English, S. McKenzie, F. Wu, E. Stark, J. Seymour, P. Ku, K. Wise, G. Buzsaki, and E. Yoon, "GaN-on-Si μ LED optoelectrodes for high-spatiotemporal-accuracy optogenetics in freely behaving animals," in *IEDM Tech. Dig.*, Dec. 2016, pp. 26.5.1–26.5.4.

[194] N. McAlinden, E. Gu, M. D. Dawson, S. Sakata, and K. Mathieson, "Optogenetic activation of neocortical neurons *in vivo* with a sapphire-based micro-scale led probe," *Frontiers Neural Circuits*, vol. 9, p. 25, May 2015.

[195] N. Dong, R. Berlinguer-Palmini, A. Soltan, N. Ponon, A. O'Neil, A. Travelyan, P. Maaskant, P. Degenaar, and X. Sun, "Opto-electro-thermal optimization of photonic probes for optogenetic neural stimulation," *J. Biophotonics*, vol. 11, no. 10, Oct. 2018, Art. no. e201700358.

[196] A. Picot, S. Dominguez, C. Liu, I.-W. Chen, D. Tanese, E. Ronzitti, P. Berto, E. Papagiakoumou, D. Oron, G. Tessier, B. C. Forget, and V. Emiliani, "Temperature rise under two-photon optogenetic brain stimulation," *Cell Rep.*, vol. 24, no. 5, pp. 1243–1253, 2018.

[197] M. Paci, E. Passini, A. Klimas, S. Severi, J. Hyttinen, B. Rodriguez, and E. Entcheva, "In silico populations optimized on optogenetic recordings predict drug effects in human induced pluripotent stem cell-derived cardiomyocytes," in *Proc. Comput. Cardiol. Conf.*, vol. 45, Dec. 2018, pp. 1–4.

[198] G. Gagnon-Turcotte, E. Maghsoudloo, Y. Messaddeq, Y. De Koninck, and B. Gosselin, "A wireless photostimulator for optogenetics with live animals," in *Proc. 15th IEEE Int. New Circuits Syst. Conf.*, Jun. 2017, pp. 193–196.

[199] L. Montazeri, N. El Zarif, T. Tokuda, J. Ohta, and M. Sawan, "Active Control of μ LED arrays for optogenetic stimulation," in *Proc. IEEE Int. Symp. Circuits Syst.*, May 2018, pp. 1–5.

[200] A. Erofeev, E. Gerasimov, A. Lavrova, A. Bol-Hakova, E. Postnikov, I. Bezprozvanny, and O. L. Vlasova, "Light stimulation parameters determine neuron dynamic characteristics," *Appl. Sci.*, vol. 9, no. 18, p. 3673, Sep. 2019.

[201] R. Schoeters, T. Tarnaud, W. Joseph, L. Martens, R. Raedt, and E. Tanghe, "Comparison between direct electrical and optogenetic subthalamic nucleus stimulation," in *Proc. World Conf. Biomed. Appl. Electromagn. Fields*, Sep. 2018, pp. 1–2.

[202] R. M. Neely, D. K. Piech, S. R. Santacruz, M. M. Maharbiz, and J. M. Carmena, "Recent advances in neural dust: Towards a neural interface platform," *Current Opinion Neurobiol.*, vol. 50, pp. 64–71, Jun. 2018.

[203] J. Charthad, T. C. Chang, Z. Liu, A. Sawaby, M. J. Weber, S. Baker, F. Gore, S. A. Felt, and A. Arbabian, "A mm-sized wireless implantable device for electrical stimulation of peripheral nerves," *IEEE Trans. Biomed. Circuits Syst.*, vol. 12, no. 2, pp. 257–270, Apr. 2018.

[204] Y. Jia, S. A. Mirbozorgi, B. Lee, W. Khan, F. Madi, O. T. Inan, A. Weber, W. Li, and M. Ghovanloo, "A mm-sized free-floating wirelessly powered implantable optical stimulation device," *IEEE Trans. Biomed. Circuits Syst.*, vol. 13, no. 4, pp. 608–618, Aug. 2019.

[205] R. Jegadeesan, S. Nag, K. Agarwal, N. V. Thakor, and Y.-X. Guo, "Enabling wireless powering and telemetry for peripheral nerve implants," *IEEE J. Biomed. Health Informat.*, vol. 19, no. 3, pp. 958–970, May 2015.

[206] P. Yeon, X. Tong, B. Lee, A. Mirbozorgi, B. Ash, H. Eckhardt, and M. Ghovanloo, "Toward a distributed free-floating wireless implantable neural recording system," in *Proc. 38th Annu. Int. Conf. IEEE Eng. Med. Biol. Soc. (EMBC)*, Aug. 2016, pp. 4495–4498.

[207] C. Kim, J. Park, S. Ha, A. Akinin, R. Kubendran, P. P. Mercier, and G. Cauwenberghs, "A 3 mm×3 mm fully integrated wireless power receiver and neural interface system-on-chip," *IEEE Trans. Biomed. Circuits Syst.*, vol. 13, no. 6, pp. 1736–1746, Dec. 2019.

[208] B. Lee, P. Yeon, and M. Ghovanloo, "A multicycle Q-modulation for dynamic optimization of inductive links," *IEEE Trans. Ind. Electron.*, vol. 63, no. 8, pp. 5091–5100, Aug. 2016.

KEONGHWAN OH (Student Member, IEEE) received the dual B.S. degrees from Northumbria University, Newcastle upon Tyne, U.K. and the Seoul National University of Science and Technology, Seoul, South Korea, in 2013., and the M.S. degree in medical science and engineering from the Gwangju Institute of Science and Technology, Gwangju, South Korea, in 2015. He is currently pursuing the Ph.D. degree in electrical engineering with the Tandon School of Engineering, New York University, New York, NY, USA. He worked at the Seoul National University of Science and Technology as a Researcher, from 2015 to 2017. He is a Graduate Research Assistant with the Integrated BioElectronics Lab, New York University Abu Dhabi, Abu Dhabi, UAE. His research interests include implantable neural interface for optical stimulation and electrocorticography (ECoG) recording with biocompatible packaging.

KAI-WEN YANG (Student Member, IEEE) received the B.S. degree *(summa cum laude)* in electrical engineering from New York University Abu Dhabi (NYUAD), UAE, in 2020. She was an Undergraduate Research Assistant with the Integrated BioElectronics Lab, NYUAD, conducting research in the field of implantable neural interface. As of September 2020, she joins the biomedical engineering program at the Johns Hopkins University, Baltimore, MD, USA, as a M.S. student. She was awarded the NYU Founders' Day Award and was elected to membership in the national honor society of Phi Beta Kappa, Beta Chapter of New York. She was part of the NYUAD 2018 team that participated in the International Genetically Engineered Machine (iGEM) Synthetic Biology Competition, and was awarded the Golden Medal, nominated Best Diagnostic Project and a Finalist.

SOHMYUNG HA (Member, IEEE) received the B.S. *(summa cum laude)* and M.S. degrees in electrical engineering from the Korea Advanced Institute of Science and Technology (KAIST), Daejeon, South Korea, in 2004 and 2006, respectively, and the M.S. and Ph.D. degrees in bioengineering from the Department of Bioengineering, University of California, San Diego, La Jolla, CA, USA, in 2015 and 2016, respectively. From 2006 to 2010, he worked at Samsung Electronics as a mixed-signal circuit designer for commercial multimedia devices. After this extended career in industry, he returned to academia as a Fulbright Scholar. Since 2016, he has been with New York University Abu Dhabi and New York University. He is currently an Assistant Professor with New York University Abu Dhabi, UAE, and a Global Network Assistant Professor of electrical and computer engineering with New York University, New York, NY, USA. His research aims at advancing the engineering and applications of silicon integrated technology interfacing with biology in a variety of forms ranging from implantable biomedical devices to unobtrusive wearable sensors. He is currently a member of the Analog Signal Processing Technical Committee of IEEE Circuits and Systems Society. He received a Fulbright Fellowship, in 2010, and the Engelson Best Ph.D. Thesis Award for Biomedical Engineering from the Department of Bioengineering, University of California, San Diego, in 2016. He has served as an Associate Editor of *Smart Health* (Elsevier) and the IEEE Transactions on Biomedical Circuits and Systems.

• • •